J. Fluid Mech. (2006), *vol.* 547, *pp.* 21–53.
doi:10.1017/S002211200500649X Printed in the United Kingdom

Leading-edge receptivity by adjoint methods

By FLAVIO GIANNETTI[1]† AND PAOLO LUCHINI[2]

[1]Department of Applied Mathematics and Theoretical Physics, University of Cambridge, Centre for Mathematical Sciences, Wilberforce Road, Cambridge CB3 0WA, UK

[2]DIMEC, Università di Salerno, Via Ponte don Melillo, 84084 Fisciano (SA), Italy

(Received 11 March 2003 and in revised form 14 June 2005)

The properties of adjoint operators and the method of composite expansion are used to study the generation of Tollmien–Schlichting (TS) waves in the leading-edge region of an incompressible, flat-plate boundary layer. Following the classical asymptotic approach, the flow field is divided into an initial receptivity region, where the unsteady motion is governed by the linearized unsteady boundary-layer equation (LUBLE), and a downstream linear amplification area, where the evolution of the unstable mode is described by the classical Orr–Sommerfeld equation (OSE). The large $\bar{x}$ behaviour of the LUBLE is analysed using a multiple-scale expansion which leads to a set of composite differential equations uniformly valid in the wall-normal direction. These are solved numerically as an eigenvalue problem to determine the local properties of the Lam and Rott eigensolutions. The receptivity coefficient for an impinging acoustic wave is extracted by projecting the numerical solution of the LUBLE onto the adjoint of the Lam and Rott eigenfunction which, further downstream, turns into an unstable TS wave. In the linear amplification region, the main characteristics of the instability are recovered by using a multiple-scale expansion of the Navier–Stokes equations and solving numerically the derived eigenvalue problems. A new matching procedure, based on the properties of the adjoint Orr–Sommerfeld operator, is then used to check the existence and the extent of an overlapping domain between the two asymptotic regions. Results for different frequencies are discussed.

1. Introduction

Among all possible linear mechanisms that are apt to excite Tollmein–Schlichting (TS) waves, the leading-edge mechanism is probably one of the most extensively studied in the last decade. The first quantitative explanation of the wavelength conversion process that takes place in the leading-edge area and tunes the unsteady disturbances in the free stream to the appropriate length-scale of the instability is due to the work of Goldstein (1983) and Ruban (1984). Performing an asymptotic analysis of the linearized Navier–Stokes equations (LNSE) in terms of the small triple-deck parameter $\epsilon_g = F^{1/6} \ll 1$, with $F = \omega^\star \nu_\infty^\star / {U_\infty^\star}^2$, Goldstein found that the unsteady motion in the boundary layer contains two different asymptotic streamwise regions. In the leading-edge area, where $\bar{x} \equiv \omega^\star x^\star / U_\infty^\star \sim O(1)$, the vertical dependence of the pressure fluctuations is negligible and the unsteady motion is governed, at leading order, by the linearized unsteady boundary-layer equations (LUBLE). In the second

† Present address: DIMEC, Università di Salerno, Via Ponte don Melillo, 84084 Fisciano (SA), Italy.

region, downstream of the leading edge, for $\bar{x} \sim O(\epsilon_g^{-2})$, the correct asymptotic approximation of the LNSE is given by a modified Orr–Sommerfeld equation (OSE), whose solutions near the neutral branch develop, in the limit of $\epsilon_g \to 0$, a triple-deck structure appropriate to interacting boundary layers. Where the two regions overlap, the behaviour of the LUBLE for $\bar{x} \to \infty$ must be asymptotically matched to the behaviour of the OSE for $\epsilon_g^2 \bar{x} \to 0$. Lam & Rott (1960, 1993) and Ackerberg & Phillips (1972) studied the asymptotic behaviour of the LUBLE for $\bar{x} \to \infty$. Exploiting its parabolic nature, they found that in the far field, the unsteady motion can be expressed as

$$\bar{\psi}(\bar{x}, \tilde{y}) \sim \bar{\psi}_p(\bar{x}, \tilde{y}) + \sum_n C_n \bar{\psi}_{c,n}(\bar{x}, \tilde{y}), \tag{1.1}$$

where $\tilde{y} \equiv (\omega^\star/\nu^\star)^{1/2} y^\star$ and $\bar{\psi}_p$ is a particular solution depending only on the local characteristics of the imposed outer inviscid flow, while $\psi_{c,n}$ are an infinite set of asymptotic eigenfunctions which account for the initial conditions. Their analytical form was determined for the first time by Lam & Rott (1960) through a matched asymptotic expansion and subsequently corrected by Goldstein (1983) to account for non-uniform mean-flow effects. They develop a two-layer structure consisting of a main inviscid layer of width $\eta = \tilde{y}\bar{x}^{-1/2} \sim O(1)$, and an inner viscous layer of width $\eta \sim O(\bar{x}^{-1/2})$.

According to the asymptotic analysis, the characteristic wavelength of the eigenfunctions shortens proportionally to $\bar{x}^{-1/2}$ in the streamwise direction. Goldstein showed that this wavelength-reduction process produces at $\bar{x} \sim O(\epsilon_g^{-2})$ significant wall-normal pressure variations which invalidate the boundary-layer approximation. In this region, the flow field is locally parallel and the unsteady perturbation turns out to be described by the classical large-wavenumber small-frequency approximation of the OSE, properly corrected to include non-parallel effects. Goldstein, using triple-deck theory, was able to find analytical asymptotic solutions of this equation. He showed that in the limit of $\epsilon_g \to 0$, the two asymptotic streamwise regions of the boundary layer have an overlap domain in which the eigenfunctions of the LUBLE match, in the sense of matched asymptotic expansion, the solutions of the OSE. There is one LUBLE eigensolution for each TS wave, but only the first one, $\bar{\psi}_{c,1}$, turns into a mode apt to become unstable further downstream. Since the whole process is linear, the final amplitude of the unstable TS wave is proportional to the coefficient of the first Lam & Rott (LR) eigenfunction: thus, the external disturbance enters into the determination of the TS amplitude only through C_1, which for this reason is called the *receptivity coefficient*.

The value of the receptivity coefficient is determined by the specific behaviour of the unsteady motion in the region $\bar{x} \sim O(1)$ and can be extracted only by performing a comparison between a numerical solution of the LUBLE and the asymptotic analytical form of the first Lam & Rott mode. Goldstein, Sockol & Sanz (1983) extracted C_1 for an incoming acoustic wave travelling parallel to the plate direction, while Heinrich (1989), Heinrich & Kerschen (1989) and Kerschen, Choudhari & Heinrich (1990) considered several types of free-stream disturbance, including convected gusts and a von Kármán vortex street passing above the boundary layer. Hammerton & Kerschen (1996, 1997) extended these calculations to a parabolic geometry in order to determine the effects of nose bluntness on the acoustic-receptivity coefficient. All these investigations were focused on the incompressible regime and restricted to simple geometric configurations, such as a flat plate or a parabola, for which an analytical

form of the Lam & Rott eigensolutions is either known or is easily determined through classical perturbation techniques. Fedorov (2003), using an asymptotic model developed by Fedorov & Khokhlov (1991, 1993), evaluated the receptivity for an acoustic wave impinging on a supersonic flat-plate boundary layer, showing that at high speed, both stable modes and the second Mack mode play a fundamental role in the process.

Extending these results to more complex flow geometries and to subsonic regimes is difficult and often requires lengthy and complex algebraic manipulations. In many cases, furthermore, the lack of suitable analytical expressions for the inviscid external flow field or the impossibility to find closed-form solutions of the asymptotic equations require a numerical determination of the properties of the eigenfunctions. Under these circumstances, two possible routes can be identified.

The first one is based on a fully numerical approach to the receptivity problem and involves determining the solution of the complete LNSE through accurate and efficient numerical schemes. In this manner, finite-Reynolds-number effects, which are usually difficult to estimate within an asymptotic approach, can be fully determined. The possibility of evaluating the TS amplitude through a direct numerical simulation of the Navier–Stokes equations (NSE) has been shown, among others, by Casalis, Gouttenoire & Troff (1997), Haddad & Corke (1998), Erturk & Corke (2001), Wanderley & Corke (2001), Zhong (2001) and by Ma & Zhong (2003*a*, *b*). The first four papers investigate the receptivity mechanism in incompressible flows for different types of leading-edge geometries, while the last three deal with the receptivity over a parabolic body or a flat plate in the supersonic regime. Despite the great potential of this method, its large memory requirements and high computational costs restrict its use to simple geometric configurations and to a certain range of Reynolds numbers which is often of poor practical interest. A detailed review of numerical and theoretical results is given by Saric, Reed & Kerschen (2002).

The second way, instead, consists in adopting a mixed approach in which standard asymptotic techniques are applied to the LNSE to derive simplified equations which are then solved numerically to determine the properties of the asymptotic solutions. Thus, we avoid the difficulties associated with a full numerical treatment of the receptivity problem and, at the same time, retain the advantages of an asymptotic approach. In this context, we have developed a new numerical procedure based on the properties of the adjoint operators, which can be successfully used to extract the receptivity coefficient and to estimate the extension of the matching region at small but finite values of the frequency parameter. This new technique is used here to study the acoustic receptivity of an incompressible flat-plate boundary layer, but can be easily implemented in more complex flow configurations or in a compressible-fluid setting.

In this paper, starting from the problem formulation, we derive the parallel stability equations from the incompressible Navier–Stokes equations by applying a standard multiple-scale analysis. Studying the solution of the OSE in a region close to the leading edge, we then derive a streamwise bound for the validity of the stability equations. A complementary asymptotic approximation of the Navier–Stokes equations is then developed in the leading-edge area; the asymptotic solutions of the resulting governing equations are studied numerically through a multiple-scale technique and a composite expansion procedure. The properties of the associated eigenfunctions are described and the eigenvalues compared with the analytic solutions found by Lam & Rott. The receptivity coefficient for an acoustic wave propagating parallel to the plate is then extracted by performing a numerical integration of the governing equations in the complex–$\bar{x}$ plane and projecting the resulting solution onto the adjoint of the Lam &

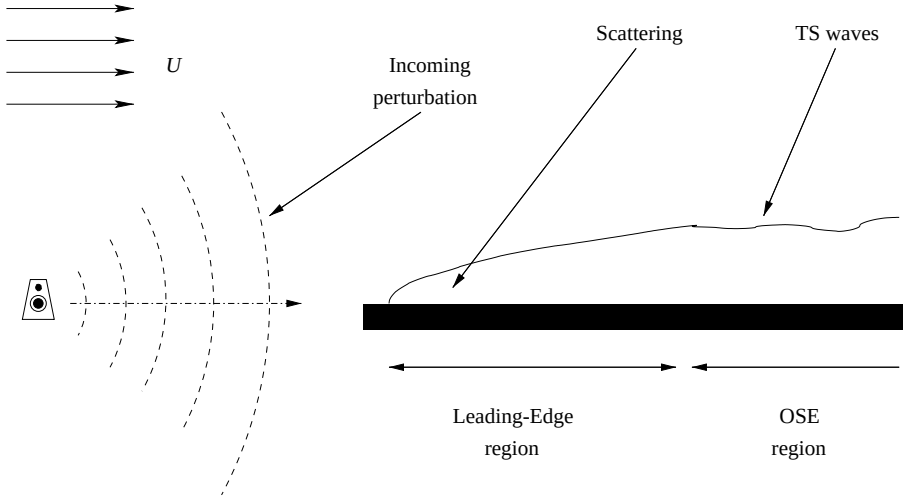

FIGURE 1. Acoustic waves impinging on a flat-plate boundary layer.

Rott mode which turns into an unstable TS wave far downstream. The properties of the higher modes are briefly discussed and the implication of their existence pointed out. A new matching procedure based on the adjoint eigenfunctions of the OSE is developed to estimate the range of validity of the leading-edge complementary approximation and to evaluate the extension of the overlap domain at small but finite values of F. Finally, this new technique is used to extract the TS amplitude at the second neutral branch for different values of the frequency parameter.

2. Problem formulation

We consider an infinite two-dimensional flat plate of zero thickness aligned to a parallel uniform stream of velocity $U^\star_\infty$. Here and in the following sections, a star identifies dimensional quantities. A weak free-stream perturbation is impinging on the plate (see figure 1) producing a small-amplitude response inside the boundary layer. The flow is described by the usual two-dimensional time-dependent Navier–Stokes equations and the frequency of the unsteady disturbance is taken to be small enough for the mean flow to support unstable TS waves. The disturbance enters the boundary layer at the leading edge and is there scattered by the non-uniform rapidly varying mean flow. The scattered field contains, among others, the correct wavelength to excite the instability waves which, as a result, appear downstream in the locally parallel region (in the picture indicated as the OSE region). If the amplitude of the external perturbation is small enough, the generation is a linear process and can be studied using linear theory. A monochromatic source, considered in a linear approximation, gives rise to a TS wavetrain of the same frequency, because in this case the dependence of all the fluid parameters on time can be separated from the very beginning when posing the initial-value problem. We therefore decompose the total unsteady field as the sum of a steady mean part and a small unsteady monochromatic perturbation of non-dimensional frequency $\omega = \omega^\star L^\star / U^\star_r$ as

$$\hat{U}(x, y, t) = U(x, y) + \epsilon_p \, u(x, y) \mathrm{e}^{\mathrm{i}\omega t}, \tag{2.1a}$$

$$\hat{V}(x, y, t) = V(x, y) + \epsilon_p \, v(x, y) \mathrm{e}^{\mathrm{i}\omega t}, \tag{2.1b}$$

$$\hat{P}(x, y, t) = P(x, y) + \epsilon_p \, p(x, y) \mathrm{e}^{\mathrm{i}\omega t}. \tag{2.1c}$$

Here, the hat denotes time-dependent quantities, $\hat{U}$ and $\hat{V}$ represent the horizontal and vertical components of the total velocity field, $\hat{P}$ is the pressure and ϵ_p denotes a small parameter ($|\epsilon_p| \ll 1$). Introducing (2.1*a*) in the governing equations and linearizing, we obtain two problems describing, respectively, the spatial evolution of the steady mean flow (U, V, P) and of the perturbation (u, v, p). In particular, the steady flow turns out to be described by the steady NSE, while the unsteady perturbation is governed by the linearized Navier–Stokes equations (LNSE)

$$\mathrm{i}\omega u + \frac{\partial(2Uu)}{\partial x} + \frac{\partial(Uv + Vu)}{\partial y} = -\frac{\partial p}{\partial x} + \frac{1}{Re}\left(\frac{\partial^2 u}{\partial x^2} + \frac{\partial^2 u}{\partial y^2}\right), \tag{2.2a}$$

$$\mathrm{i}\omega v + \frac{\partial(Uv + Vu)}{\partial x} + \frac{\partial(2Vv)}{\partial y} = -\frac{\partial p}{\partial y} + \frac{1}{Re}\left(\frac{\partial^2 v}{\partial x^2} + \frac{\partial^2 v}{\partial y^2}\right), \tag{2.2b}$$

$$\frac{\partial u}{\partial x} + \frac{\partial v}{\partial y} = 0. \tag{2.2c}$$

Equations (2.2*a*) are made dimensionless with respect to a reference velocity $U_r^\star$, a reference length scale $L_r^\star$ and a pressure scale $\rho_\infty^\star U_r^{\star 2}$, with $\rho_\infty^\star$ indicating the free-stream value of the density. The dimensionless parameter Re appearing in the equations is the Reynolds number based on $L_r^\star$ and is defined as

$$Re = \frac{U_r^\star L_r^\star}{\nu_\infty^\star}, \tag{2.3}$$

where $\nu_\infty^\star$ denotes the kinematic viscosity. Both the steady NSE and the LNSE must be supplemented with suitable boundary conditions. In particular, on the surface of the plate, which is assumed to have its leading edge centred at $x = 0,\ y = 0$, the no-slip and no-penetration conditions require both the steady and unsteady velocity components to vanish ($U = V = u = v = 0$), while far away from the plate we assume that

$$U(x, y) \to 1, \quad V(x, y) \to 0, \tag{2.4a}$$

$$u(x, y) \to u_\infty(x, y), \quad v(x, y) \to v_\infty(x, y), \tag{2.4b}$$

where $u_\infty(x, y)$ and $v_\infty(x, y)$ are the far-field values of the impinging unsteady disturbance. Although both the steady and unsteady problems can, in principle, be solved by a direct numerical simulation, this will not be attempted here. Making use of asymptotic techniques, we will derive simplified equations which describe the asymptotic behaviour of the NSE and which can be more easily solved either analytically or numerically.

3. Notation

For a flat-plate boundary layer, a convenient choice to non-dimensionalize the governing equations is to identify the reference velocity $U_r^\star$ with the free-stream value $U_\infty^\star$ and to take as the reference length scale $L_r^\star$ either a given distance $x_r^\star$ from the leading edge, a characteristic boundary-layer thickness $\delta_r^\star = \sqrt{x_r^\star \nu_\infty^\star / U_\infty^\star}$ or the convective length scale $l_c^\star = U_\infty^\star / \omega^\star$. Since in this paper we study the receptivity problem separating the flow field into various asymptotic regions where different types of approximation and scalings hold, it is convenient to use more than one choice of $L_r^\star$ and employ different notations for each. In particular, we adopt lower case letters (as $x, y, \alpha, \omega, \ldots$) and lower case over-barred letters (as $\bar{x}, \bar{y}, \bar{\alpha}, \ldots$) to indicate quantities

Boundary layer thickness	Convective scale	Base flow scale	Tollmein–Schlichting wavelength	Lam & Rott wavelength
$\delta_r^\star \equiv \sqrt{\frac{x_r^\star \nu}{U_\infty^\star}}$	$\ell_c^\star \equiv \frac{U_\infty^\star}{\omega^\star}$	$\ell_B^\star \equiv x_r^\star$	$\ell_{TS}^\star$	$\ell_{LR}^\star$

TABLE 1. Characteristic scales.

Re	R_x	F	Sr	ε	τ	ϵ_1	ϵ_2
$\frac{\delta_r^\star U_\infty^\star}{\nu^\star}$	Re^2	$\frac{\omega^\star \nu^\star}{{U_\infty^\star}^2}$	$\frac{\omega^\star x_r^\star}{U_\infty^\star}$	$\frac{1}{Re}$	$\frac{1}{Sr}$	$\frac{\ell_{TS}^\star}{\ell_B^\star}$	$\frac{\ell_{LR}^\star}{\ell_B^\star}$

TABLE 2. Dimensionless parameters.

x	y	$\bar{x}$	$\bar{y}$	$\tilde{y}$	X	X_1	X_2
$\frac{x^\star}{\delta_r^\star}$	$\frac{y^\star}{\delta_r^\star}$	$\frac{x^\star}{\ell_c^\star}$	$\frac{y^\star}{\ell_c^\star}$	$y^\star\sqrt{\frac{\omega^\star}{\nu^\star}}$	εx	$\epsilon_1 x$	$\epsilon_2 \bar{x}$

TABLE 3. Dimensionless quantities.

non-dimensionalized, respectively, on the characteristic boundary-layer thickness $\delta_r^\star$ and on the convective wavelength $\ell_c^\star$, while the symbols X, X_1, X_2 are used to indicate the rescaled streamwise coordinate (see tables 1, 2, 3 for details). The non-dimensional frequency parameter F, defined as the inverse of the Reynolds number based on $\ell_c^\star$,

$$F = \frac{\omega^\star \nu_\infty^\star}{U_r^{\star 2}}, \tag{3.1}$$

is related to the common Reynolds numbers Re and R_x, respectively based on the boundary-layer thickness $\delta_r^\star$ and on the distance from the leading edge $x_r^\star$, by

$$Sr = F\,Re^2 = F\,R_x, \tag{3.2}$$

where the Strouhal number Sr is defined as

$$Sr = \frac{\omega^\star x_r^\star}{U_\infty^\star}\ . \tag{3.3}$$

According to (3.2), the two limiting processes $F \to 0$ and $Re \to \infty$ are equivalent if $Sr \sim O(1)$: in particular when $Sr = 1$ we obtain $Re \equiv 1/\sqrt{F}$ and $\bar{x} \equiv X$. Linear stability theory shows that unstable TS waves are supported by the mean flow only if F is below a certain threshold which is usually small: thus, without any loss of generality, we will assume $F \ll 1$. In this case, a viscous length smaller than $l_c^\star$ enters into play and a re-scaled vertical coordinate,

$$\tilde{y} = \frac{1}{\sqrt{F}}\,\bar{y} \equiv y^\star\sqrt{\omega^\star/\nu^\star}, \tag{3.4}$$

is sometime used to describe the properties of the unsteady viscous boundary layer better. Choosing $Sr = 1$ implies that $\tilde{y} \equiv y$. Other symbols used in this paper and appearing in tables 1, 2 and 3 will be introduced in due course. Finally, the action of

a given functional g on an element f is indicated with the standard notation

$$g(f) = \langle g\,,\ f\rangle = \int_0^\infty g\, f\, \mathrm{d}y, \tag{3.5}$$

while the adjoint $\mathscr{L}^\dagger$ of a differential operator $\mathscr{L}$ is defined as the unique operator satisfying

$$\langle v\,,\ \mathscr{L}\, u\rangle - \langle \mathscr{L}^\dagger v\,,\ u\rangle = 0 \tag{3.6}$$

for any pair of suitable differentiable real or complex fields u and v. Equation (3.6) is supposed to hold in the distribution sense, where for distributions we intend functionals on a suitable space of test functions.

4. Mean flow

For $Re \gg 1$, the steady flow can be approximated using Prandtl' s boundary-layer theory. On introducing the small parameter $\varepsilon = Re^{-1}$ and the slow variable $X = \varepsilon x$, the inner expansion of the boundary-layer approximation can be written in terms of the stream function Ψ as

$$\Psi(X, y) = \Psi_0(X, y) + \varepsilon\Psi_1(X, y) + \text{h.o.t.} \tag{4.1}$$

If (4.1) is introduced in the steady NSE rewritten in terms of Ψ, the solution of the leading-order problem can be written as

$$\Psi_0(X, y) = \sqrt{X} f(\eta), \tag{4.2}$$

where $\eta = y/\sqrt{(X)}$ is the similarity variable and f satisfies the well-known Blasius equation

$$\left.\begin{aligned} &f''' + \tfrac{1}{2} f f'' = 0, \\ &f(0) = f'(0) = 0, \\ &f'(\eta) \to 1 \quad as\eta \to \infty. \end{aligned}\right\} \tag{4.3}$$

Higher-order correction terms can be found solving the second-order inner and outer problems (Van Dyke 1964). In particular, Goldstein (1956, 1960) showed that for a semi-infinite flat plate, Ψ_1 vanishes and the inner solution (4.2) is accurate up to $O(\varepsilon^2 \log(\varepsilon^{-1}))$. In this case, the steady solution of the Navier–Stokes equations takes on the form

$$U(X, y) = U_B(X, y) + O(\varepsilon^2 \log(\varepsilon^{-1})), \tag{4.4a}$$

$$V(X, y) = \varepsilon V_B(X, y) + O(\varepsilon^3 \log(\varepsilon^{-1})), \tag{4.4b}$$

$$P(X, y) = O(\varepsilon^2 \log(\varepsilon^{-1})), \tag{4.4c}$$

where $U_B(X, y) \equiv \partial\Psi_0/\partial y = f'(\eta)$ and $V_B(X, y) \equiv -\partial\Psi_0/\partial X = 0.5\,[\eta f'(\eta) - f(\eta)]/\sqrt{X}$. Blasius' equation (4.3) is solved numerically using a fourth-order Runge–Kutta scheme.

5. The OSE region: a finite-Reynolds-number approach

The receptivity takes place in the leading-edge area, where the external unsteady perturbation penetrates into the boundary layer and is there scattered by the rapidly developing mean flow. This process excites TS waves which, as a result, appear in the quasi-parallel region located further downstream. Here, the base flow (4.4) evolves on a characteristic length scale much larger than the typical wavelength of the perturbation, so that a multiple-scale approximation (Bender & Orszag 1978;

Hinch 1994) can be used to study the evolution of the instability. Roughly speaking, two different procedures are available to perform such an asymptotic analysis. One possibility is to use a *classical* asymptotic approach in which all the flow quantities are approximated using Poincaré expansions (see Hinch 1994, p. 25). In the present case, this procedure leads to a singular problem and to a multi-deck formulation: the boundary layer is divided into different vertical regions which are treated separately after re-scaling the dependent and the independent variables. A compound solution is then derived through the theory of matched asymptotic expansions. For example, in the vicinity of the lower branch of the neutral curve, the flow field develops a typical triple-deck structure (Stewartson 1969, 1974; Smith 1979*a, b*) consisting of an outer irrotational deck of $O(Re^{3/4}\delta_r^\star)$, an inviscid but rotational main deck of $O(\delta_r^\star)$ and an inner viscous layer of $O(Re^{1/4}\delta_r^\star)$. The triple-deck expansion, although formally correct, converges (in an asymptotic sense) too slowly to be used for quantitative predictions in common practical applications: the leading-order term of the series, in fact, rarely provides the necessary accuracy when the Reynolds number is only moderately large. Moreover, the expansion is not uniformly valid in the streamwise direction: it can be shown, in fact, that near the upper branch of the neutral curve, the boundary layer develops a more complex five-deck structure (Bodonyi & Smith 1981), where a different set of scalings applies. The multi-deck approach is the preferred route when an exact or approximate analytical solution of the problem is desired. On the other hand, when a simple numerical solution is sought, a more convenient approach consists in using a *composite asymptotic expansion*, i.e. an expansion in which both the gauge functions and their coefficients (which are themselves functions of the non-limiting variables) depend on the asymptotic parameter (Hinch 1994, p. 25; Van Dyke 1964, p. 195). For singular problems, this procedure leads to simplified equations which are uniformly valid over the entire domain and which can be solved with standard numerical techniques. In this way the difficulties and the technicalities involved with the classical multi-deck approach are easily bypassed. By its own nature, this type of expansion is not unique since a certain freedom is left in setting up the leading and the higher-order problems. This approach has been successfully adopted by Gaster (1974) and by Saric & Nayfeh (1975) to study the streamwise evolution of the TS waves on a flat-plate boundary layer. Bottaro & Luchini (1999) used a similar procedure to study the instability of Görtler vortices.

In this paper, we shall rely on the second approach, which is easier to use and is more accurate at moderate Reynolds numbers. In order to perform a multiple scale analysis we define a new expansion parameter ϵ_1 as the ratio of the two main length scales occurring in the problem, i.e.

$$\epsilon_1 = \frac{\ell_{TS}^\star}{\ell_B^\star}. \tag{5.1}$$

Here, $\ell_B^\star \equiv x_r^\star$ is the characteristic scale over which the base flow experiences an $O(1)$ change, while $\ell_{TS}^\star$ is the characteristic wavelength of the perturbation. A classical multi-deck approach (Stewartson 1969, 1974; Smith 1979*a, b*; Bodonyi & Smith 1981) shows that $\ell_{TS}^\star$ is asymptotically larger than the boundary-layer thickness $\delta_r^\star$, but asymptotically smaller than the convective wavelength $\ell_c^\star$. More precisely, $\ell_{TS}^\star \sim Re^{-q}\,\ell_c^\star \sim Re^q\,\delta_r^\star$, where the value of q varies from 1/4 in the proximity of the lower branch of the neutral stability curve to 1/10 on the upper branch. Gaster (1974) and Saric & Nayfeh (1975) in deriving their stability equations assumed $\ell_{TS}^\star \sim \delta_r^\star$ and $\ell_{TS}^\star/\ell_c^\star \sim O(1)$, a choice which leads to $\epsilon_1 = \varepsilon \ll 1$ and $\omega \sim O(1)$. In this paper, instead, in order to derive an asymptotic approximation which is uniformly valid both

in the streamwise and cross-stream directions, we take $\epsilon_1 \ll 1$ with $\epsilon_1 \sim O(\varepsilon)$, but without further assumptions on the relative order of magnitude of the two parameters. We then perform a multiple-scale expansion non-dimensionalizing the LNSE (2.2*a*) on the local boundary-layer thickness $\delta_r^\star$ and seeking a short-wavelength asymptotic solution of the form

$$\boldsymbol{q}(X_1, y) = \exp(-\mathrm{i}\phi(X_1)/\epsilon_1) \sum_n \boldsymbol{q}_n(X_1, y; \epsilon_1)\epsilon_1^n, \tag{5.2}$$

where the slow variable $X_1 = \epsilon_1 x$ is kept $O(1)$ in the limit $\epsilon_1 \to 0$. Note that expansion (5.2) depends on both ϵ_1 and ε, owing to the base flow dependence on the Reynolds number. For our purpose, it is not necessary to provide an explicit relation between the two asymptotic parameters since, as Govindarajan & Narasimha (1997, 1999, 2001) and Narasimha & Govindarajan (2000) showed, such a link is required only to derive more accurate approximations which are, however, not required in this paper. In (5.2), $\boldsymbol{q} = [u, v, p]^t$ is the vector containing the field components, while ϕ is a function of X_1 to be determined during the asymptotic procedure. Introducing (5.2) and the base flow expansion (4.4) in the governing equations, retaining at most terms of $O(\varepsilon)$ and collecting like powers of ϵ_1, we are left with the following series of problems describing the evolution of the perturbation inside the boundary layer

$O(\epsilon_1^0)$

$$\boldsymbol{H}_{OS}(\alpha, \omega, Re)\, \boldsymbol{q}_0(X_1, y) = 0, \tag{5.3a}$$

$$u_0, v_0, p_0 \to 0 \qquad \text{as } y \to \infty, \tag{5.3b}$$

$$u_0 = v_0 = 0 \qquad \text{at } y = 0, \tag{5.3c}$$

$O(\epsilon_1^1)$

$$\boldsymbol{H}_{OS}(\alpha, \omega, Re)\boldsymbol{q}_1(\boldsymbol{X}_1, y) = -\boldsymbol{M}(\alpha, Re, \epsilon_1)\boldsymbol{q}_0 - \boldsymbol{L}(\alpha, Re)\frac{\mathrm{d}\boldsymbol{q}_0}{\mathrm{d}X_1}, \tag{5.4a}$$

$$u_1, v_1, p_1 \to 0 \qquad \text{as } y \to \infty, \tag{5.4b}$$

$$u_1 = v_1 = 0 \qquad \text{at } y = 0. \tag{5.4c}$$

Here,

$$\alpha = \frac{\mathrm{d}\phi}{\mathrm{d}X_1} \tag{5.5}$$

is the wavenumber of the perturbation, $\boldsymbol{H}_{OS}(\alpha, \omega, R)$ is the classical Orr–Sommerfeld operator and $\boldsymbol{L}(\alpha, Re)$ and $\boldsymbol{M}(\alpha, Re, \epsilon_1)$ are operators accounting for the slow streamwise growth of the boundary layer whose explicit form is given in detail in Appendix A. Equation (5.3*a*), with its homogeneous boundary conditions, is an eigenvalue problem for the determination of the eigenvalue α and its corresponding eigenvector $\boldsymbol{q}_0$. It is well known that, for a given Reynolds number Re, the OSE admits only a finite number of discrete eigenvalues. Grosch & Salwen (1978, 1981) showed that, in addition to the discrete spectrum, the operator $\boldsymbol{H}_{OS}$ admits a continuous spectrum composed of bounded eigenfunctions which are not square-integrable in y. These generalized modes decay in the streamwise direction, so that they can be ignored in a receptivity context. For a fixed frequency, the number of discrete modes supported by the mean flow usually increases with the Reynolds number. Among them only one becomes unstable (i.e. its eigenvalue has a positive imaginary part: $\alpha^{(i)} > 0$) in a certain region of the frequency–Reynolds number plane: this mode represents the unstable TS wave.

The solution of the vector equation (5.3) determines the leading-order term of expansion (5.2) up to an arbitrary function of the streamwise coordinate X_1. Writing

$$\boldsymbol{q}_0(X_1, y) = A(X_1)\boldsymbol{u}_0(X_1, y) + O(\epsilon_1, \varepsilon), \tag{5.6}$$

where $\boldsymbol{u}_0$ is a convenient normalization of the eigenfunction, we can uniquely determine the amplitude function $A(X_1)$ by imposing a solvability condition on the second-order problem (5.4). This is, in fact, a singular problem and therefore a solution exists only if the forcing term on the right-hand side of (5.4) belongs to the kernel of the adjoint solution $\boldsymbol{v}_0$, i.e. if

$$\left\langle \boldsymbol{v}_0, \boldsymbol{L}(\alpha, Re)\frac{\mathrm{d}\boldsymbol{q}_0}{\mathrm{d}X_1} + \boldsymbol{M}(\alpha, \epsilon_1, Re)\boldsymbol{q}_0 \right\rangle = 0. \tag{5.7}$$

Using (5.6) to solve (5.7) and expressing the results in terms of the slow streamwise variable X, the leading-order approximation of the LNSE assumes the following form

$$\boldsymbol{q}_n(X, y) = A_n(X_i)\boldsymbol{u}_{0,n} \exp\left[-\frac{\mathrm{i}}{\varepsilon}\int_{X_i}^{X} \kappa_n \mathrm{d}X \right] + O(\epsilon_1, \varepsilon), \tag{5.8}$$

where the subscript n refers to the mode number, X_i denotes some given initial streamwise position, $A_n(X_i)$ is the value assumed by the amplitude A_n at that location and where the wavenumber

$$\kappa_n \equiv \alpha_n + \Delta\alpha_n = \alpha_n - \epsilon_1 \,\mathrm{i}\, \frac{\left\langle \boldsymbol{v}_0, \boldsymbol{L}\dfrac{\mathrm{d}\boldsymbol{u}_0}{\mathrm{d}X_1} + \boldsymbol{M}\boldsymbol{u}_0 \right\rangle}{\langle \boldsymbol{v}_0, \boldsymbol{L}\boldsymbol{u}_0 \rangle} \tag{5.9}$$

accounts for non-parallel mean-flow effects. In a similar way, it is possible to show that

$$\boldsymbol{q}_n^{\dagger}(X, y) = \boldsymbol{v}_{0,n} \exp\left[\frac{\mathrm{i}}{\varepsilon}\int_{X_0}^{X} \kappa_n \mathrm{d}X \right] + O(\epsilon_1, \varepsilon) \tag{5.10}$$

represents the approximate solution of the adjoint problem governed by the adjoint linearized Navier–Stokes operator. It should be noted that these solutions have been derived without any particular assumption on the relative order of magnitude of ϵ_1 and ε. A more accurate result can be obtained if a link between the two asymptotic parameters is provided. Such a relation always be can retrieved at a given streamwise position from a numerical investigation of the eigenvalue problem (5.3).

6. Numerical solution of the Orr–Sommerfeld equation

The stability equations (5.3) are discretized by fourth-order central differences over a smoothly varying mesh in which the pressure p is staggered by a half y step with respect to u and v. The two second-order momentum equations are collocated at the same position as u and v, while the first-order continuity equation is discretized at the pressure nodes. The resulting algebraic equations are recast in the matrix formulation

$$\boldsymbol{H}(\alpha, \omega, Re)\,\boldsymbol{u} = \boldsymbol{0}, \tag{6.1}$$

where $\boldsymbol{H}$ represents now a block penta-diagonal banded matrix and $\boldsymbol{u}$ is a vector containing all the unknowns at their respective grid locations. It is useful here to retain the notation employed for the continuous problem: in this way, in fact, most of the equations derived in the previous section continue to hold after discretization, provided that each term is properly interpreted. The wall boundary conditions are

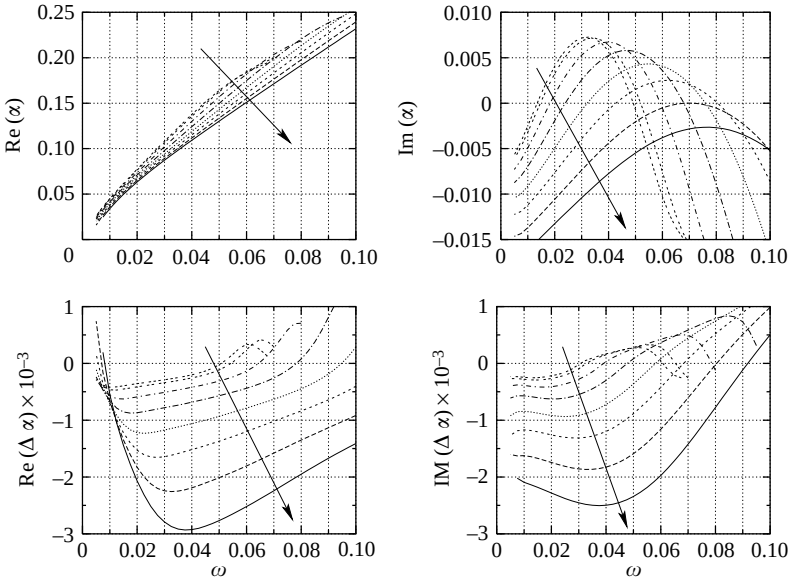

FIGURE 2. First mode eigenvalue and its correction for different values of ω. Both wavenumber and frequency are non-dimensionalized on the boundary-layer thickness. The Reynolds number corresponding to each line increases in the arrow's direction according to the sequence $Re = 230, 302, 420, 580, 850, 1250, 1750, 2000$.

inserted in the first rows of matrix $\boldsymbol{H}$, while the last rows account for the analytically determined asymptotic behaviour of (5.3*a*) as $y \to \infty$. The resulting algebraic problem is solved numerically by a variant of the classical inverse-iteration algorithm to determine the eigenvalue α and the right and left (adjoint) eigenvectors $\boldsymbol{u}$ and $\boldsymbol{v}$.

Some results used to validate the code are given in figure 2, which shows the wavenumber α of the unstable mode and its non-parallel correction $\Delta\alpha$ for different values of the flow parameters. Note that $\Delta\alpha$ is not an absolute quantity but depends on the particular normalization used: here, the right and left eigenvectors are normalized requiring

$$|u(y)|_{max} = 1; \qquad \langle \boldsymbol{v}, \boldsymbol{L}\boldsymbol{u} \rangle \equiv \left\langle \boldsymbol{v}, \mathrm{i}\frac{\partial \boldsymbol{H}_{OS}}{\partial \alpha}\boldsymbol{u} \right\rangle = 1. \tag{6.2}$$

7. LUBLE and Lam & Rott eigenfunctions

The asymptotic expansion (5.2) and consequently the stability equations (5.3) and (5.4) become invalid when the expansion parameter ϵ_1 assumes $O(1)$ values, i.e. when $\alpha \sim O(\varepsilon)$. In order to locate better the region where this occurs, it is convenient to assume an *a priori* estimate for the perturbation wavelength ℓ_{TS}. Numerical solutions of the OSE at different frequencies show that $\ell^\star_{TS}/\ell^\star_c \sim O(1)$, an estimate which was also used by Saric & Nayfeh (1975) and which is confirmed by the more refined results obtained through the multi-deck approach. Assuming such scaling, it is now easy to show that the OSE is surely not valid in the region of the flow field where

$$Sr \equiv \frac{\omega^\star x^\star_r}{U^\star_\infty} \sim O(1), \tag{7.1}$$

i.e. at distances from the leading edge comparable to the convective wavelength. In this area of the boundary layer, $\omega \sim O(\varepsilon)$ while $F \sim O(\varepsilon^2)$. The parallel-flow assumption is invalid there since the base flow evolves rapidly in the streamwise direction. Terms accounting for the vertical mean flow velocity component, neglected in the derivation of the OSE, must be included at leading order if the flow has to be resolved properly. In order to study the receptivity process without relying on a full numerical simulation of the LNSE, we proceed by simplifying the governing equations with a complementary asymptotic approximation. The limits for which this new approximation must be found are:

$$\frac{\mathrm{d}}{\mathrm{d}x} \ll \frac{\mathrm{d}}{\mathrm{d}y}, \tag{7.2a}$$

$$\varepsilon \ll 1 \quad \text{with} \quad Sr \sim O(1). \tag{7.2b}$$

From (7.2*a*), the perturbation has different evolution scales in the streamwise and vertical direction, while (7.2*b*) with (3.2) shows that the Reynolds number based on the convective length scale is large and consequently viscous effects are confined in a small layer close to the wall. In order to derive a new set of equations describing the evolution of the perturbation in the leading-edge area, we therefore use a boundary-layer approximation, whose inner expansion assumes the usual form

$$u = u_0 + \varepsilon u_1 + \varepsilon^2 u_2 + \ldots, \tag{7.3a}$$

$$v = \varepsilon[\tilde{v}_0 + \varepsilon^2 \tilde{v}_1 + \varepsilon^2 \tilde{v}_2 + \ldots], \tag{7.3b}$$

$$p = p_0 + \varepsilon p_1 + \varepsilon^2 p_2 + \ldots. \tag{7.3c}$$

Introducing (7.3) into (2.2*a*), rescaling the streamwise coordinate as $x = X/\varepsilon$ and passing to the limit $\varepsilon \to 0$ while holding $Sr \sim O(1)$, we obtain at leading order the following unsteady linearized boundary-layer equations (LUBLE):

$$\mathrm{i}\, Sr\, u_0 + \frac{\partial u_0}{\partial X} U_B + \frac{\partial U_B}{\partial X} u_0 + \frac{\partial u_0}{\partial y} V_B + \frac{\partial U_B}{\partial y} \tilde{v}_0 = -\frac{\partial p_\infty}{\partial X} + \frac{\partial^2 u_0}{\partial y^2}, \tag{7.4a}$$

$$\frac{\partial p_0}{\partial y} = 0, \tag{7.4b}$$

$$\frac{\partial u_0}{\partial X} + \frac{\partial \tilde{v}_0}{\partial y} = 0, \tag{7.4c}$$

with initial and boundary conditions given by

$$u_0 = \tilde{v}_0 = 0 \qquad \text{at } y = 0\,(X > 0), \tag{7.5a}$$

$$u_0 \to u_\infty^{(e)}(X),\ p_0^{(e)} \to p_\infty(X) \qquad \text{as } y \to \infty\,(X > 0), \tag{7.5b}$$

$$u_0(X, y) = u_{in}(y) \qquad \text{at } X = 0 \quad \forall y. \tag{7.5c}$$

Note that the solution of (7.4) does not depend on the particular value of Sr which is only determined by the non-dimensionalization used. In particular, when $\ell_c^\star$ is taken as the reference length scale, we obtain $Sr = 1$, $\bar{x} \equiv X$ and $y \equiv \tilde{y}$. Although this is the most convenient choice, we retain here the formal parameter Sr since this will be useful in setting up a multiple-scale expansion of the LUBLE using the approach adopted for the OSE. In the following zero the, subscripts, referring to the leading-order term in (7.3), will be neglected for notation convenience. The functions $u_\infty^{(e)}(X)$ and $p_\infty^{(e)}(X)$ are, respectively, the slip velocity and the pressure distribution imposed by the external inviscid problem governed by the linearized unsteady Euler equations, while $u_{in}(y)$ is an appropriate initial condition used to solve the PDE. The LUBLE are a set

of parabolic partial differential equations whose streamwise asymptotic behaviour is expressible as the sum of a particular solution, which depends on the characteristics of the outer inviscid field, and a series of asymptotic eigenfunctions, which account for the imposed initial conditions. Here, the characteristics of these asymptotic flow components are studied using a multiple-scale approximation which allows us to derive a uniformly valid composite ordinary differential equation describing the local properties of the unsteady motion. In order to perform the asymptotic analysis, we assume that downstream of the leading edge, in a region where $\tau \equiv Sr^{-1} \ll 1$, the unsteady perturbation evolves on a length scale $\ell^\star_{LM}$ much smaller than the typical evolution scale $\ell^\star_B \equiv x^\star_r$ of the base flow. Introducing the small parameter ϵ_2

$$\epsilon_2 = \frac{\ell^\star_{LR}}{\ell^\star_B} \ll 1 \tag{7.6}$$

and the scaled variable $X_2 = \epsilon_2 \bar{x} = \epsilon_2 Sr\, X$, we rewrite (7.4) in the compact vectorial notation

$$\epsilon_2 \boldsymbol{D} \frac{\partial \tilde{\boldsymbol{q}}}{\partial X_2} + [\boldsymbol{B}_1(Sr) + \epsilon_2 \boldsymbol{B}_2(Sr, \epsilon_2)]\tilde{\boldsymbol{q}} = \tilde{\boldsymbol{h}}, \tag{7.7}$$

where $\tilde{\boldsymbol{q}} \equiv [u, \tilde{v}, p]^t$ is the vector containing all the unknowns, $\tilde{\boldsymbol{h}} = [-\epsilon_2(\partial p_\infty/\partial X_2), 0, 0]^t$ is a forcing term and $\boldsymbol{D}$, $\boldsymbol{B}_1$ and $\boldsymbol{B}_2$ are operators whose explicit form is given in Appendix B. In order to determine the characteristics of the Lam & Rott eigenfunctions we assume now $\epsilon_2 \sim O(\tau)$ without specifying any further relation between the two parameters. We then seek a homogeneous solution of (7.7) by imposing a multiple-scale expansion of the form

$$\tilde{\boldsymbol{q}}(X_2, y) = \exp(-\mathrm{i}\Theta(X_2)/\epsilon_2) \sum_n \tilde{\boldsymbol{q}}_n(X_2, y, \epsilon_2)\, \epsilon_2^n \qquad \text{as} \quad \epsilon_2 \to 0, \tag{7.8}$$

Note that expansion (7.8) depends formally on both parameters ϵ_2 and τ. Substituting (7.8) into (7.5) and collecting like powers of ϵ_2, we obtain the following problems describing the far-field behaviour of the LUBLE:

$O(\epsilon_2^0)$

$$[\boldsymbol{B}_1(Sr) - \mathrm{i}\bar{\alpha}\boldsymbol{D}]\tilde{\boldsymbol{q}}_0(X_2, y) = \boldsymbol{0}, \tag{7.9a}$$

$$u_0, p_0 \to 0 \qquad \text{as } y \to \infty, \tag{7.9b}$$

$$u_0, \tilde{v}_0 = 0 \qquad \text{at } y = 0, \tag{7.9c}$$

$O(\epsilon_2^1)$

$$[\boldsymbol{B}_1(Sr) - \mathrm{i}\bar{\alpha}\boldsymbol{D}]\tilde{\boldsymbol{q}}_1(X_2, y) = -\boldsymbol{B}_2(Sr, \epsilon_2)\tilde{\boldsymbol{q}}_0 - \boldsymbol{D}\frac{\mathrm{d}\tilde{\boldsymbol{q}}_0}{\mathrm{d}X_2} \tag{7.10a}$$

$$u_1, p_1 \to 0 \qquad \text{as } y \to \infty \tag{7.10b}$$

$$u_1, \tilde{v}_1 = 0 \qquad \text{at } y = 0, \tag{7.10c}$$

where

$$\bar{\alpha} = \frac{\mathrm{d}\Theta}{\mathrm{d}X_2} \tag{7.11}$$

is the wavenumber of the perturbation non-dimensionalized on the convective length scale $\ell^\star_c$. The system (7.9) represents, once again, an eigenvalue problem whose solutions are the celebrated Lam & Rott eigenfunctions. With the specific $\bar{\alpha}$ obtained

from (7.9), the second-order problem (7.10) is singular and the solvability condition,

$$\left\langle \tilde{\boldsymbol{v}}_0, \boldsymbol{B}_2\tilde{\boldsymbol{u}}_0 + \boldsymbol{D}\frac{\mathrm{d}\tilde{\boldsymbol{u}}_0}{\mathrm{d}X_2} \right\rangle = 0, \tag{7.12}$$

must be imposed in order to guarantee the existence of the solution. The adjoint eigenvector $\tilde{\boldsymbol{v}}_0 \equiv \tilde{\boldsymbol{u}}_0^{\dagger}$ satisfies the adjoint problem, which is derived applying the definition (3.6) to the operator $[\boldsymbol{B}_1 - \mathrm{i}\bar{\alpha}\boldsymbol{D}]$ and integrating by parts. Setting

$$\tilde{\boldsymbol{q}}_0(X_2, y) = C(X_2)\tilde{\boldsymbol{u}}_0(X_2, y) + O(\epsilon_2, \tau), \tag{7.13}$$

where $\tilde{\boldsymbol{u}}_0$ indicates some suitable normalization of the eigenvector, solving (7.12) and expressing the results in terms of the slow variable $X = \tau\bar{x}$, the solution of problems (7.9) and (7.10) can be expressed as

$$\tilde{\boldsymbol{q}}(X, y) = \underbrace{C(X_i)\exp\left[-\frac{\mathrm{i}}{\tau}\int_{X_i}^{X}\bar{\kappa}\mathrm{d}X\right]}_{T^{(LR)}(X)}\tilde{\boldsymbol{u}}_0 + O(\epsilon_2, \tau). \tag{7.14}$$

Here, $X_i = \tau\bar{x}_i$ is some given initial position, $C(X_i)$ is the value of the amplitude at $X = X_i$ and the wavenumber

$$\bar{\kappa} = \bar{\alpha} + \Delta\bar{\alpha} = \bar{\alpha} - \mathrm{i}\epsilon_2\frac{\left\langle \tilde{\boldsymbol{v}}_0, \boldsymbol{D}\dfrac{\mathrm{d}\tilde{\boldsymbol{u}}_0}{\mathrm{d}X_2} + \boldsymbol{B}_2\tilde{\boldsymbol{u}}_0 \right\rangle}{\left\langle \tilde{\boldsymbol{v}}_0, \boldsymbol{D}\tilde{\boldsymbol{u}}_0 \right\rangle}, \tag{7.15}$$

includes now non-parallel mean-flow effects. The determination of the Lam & Rott eigenfunctions with this procedure is easy and does not require the detailed knowledge of the asymptotic structure of the base flow. Also, it offers in a single step a uniformly valid asymptotic approximation to the cost of the numerical solution of an eigenvalue problem. Using previous results, the solution of the LNSE in the leading-edge area can be expressed as

$$\boldsymbol{q}_n(X, y) = C_n(X_i)\,\boldsymbol{u}_{0,n}\,\exp\left[-\frac{\mathrm{i}}{\varepsilon}\int_{X_i}^{X}\kappa_n\mathrm{d}X\right] + O\left(\epsilon_2, \tau, F^{1/2}\right), \tag{7.16}$$

with $\kappa_n = \varepsilon\bar{\kappa}_n/\tau$ and $\boldsymbol{u}_{0,n} = [\mathrm{u}_{0,n}, \varepsilon\tilde{\mathrm{v}}_{0,n}, 0]^t$ and where the index n refers to the mode number.

8. Properties of the LUBLE eigenfunctions

The governing equations describing the behaviour of the Lam & Rott eigensolutions represent a classical generalized linear eigenvalue problem. Modes belonging to this class satisfy 'biorthogonality relations' deriving from the properties of the adjoint operators (Morse & Feshbach 1953, p. 884). In particular, using a proper normalization for the right-hand and left-hand eigenvectors of the LUBLE, we can write

$$\left\langle \tilde{\boldsymbol{v}}_{0,n}, \boldsymbol{D}\tilde{\boldsymbol{u}}_{0,m} \right\rangle = \int_0^{\infty}\tilde{\boldsymbol{v}}_{0,n}\cdot\boldsymbol{D}\tilde{\boldsymbol{u}}_{0,m}\mathrm{d}y = \delta_{m,n}, \tag{8.1}$$

where the second index refers to the mode number and $\delta_{m,n}$ is the Kronecker delta symbol. Equation (8.1) can be extended to define biorthogonality relations among all the eigenfunctions, including those belonging to the continuous spectrum of the operator $[\boldsymbol{B}_1 - \mathrm{i}\bar{\alpha}\boldsymbol{D}]$. The continuous modes of the LUBLE are characterized by a horizontal velocity component which does not decay in the wall-normal direction,

but remains bounded as $y \to \infty$; this property is often useful to model free-stream disturbances entering the boundary layer (for example the Stokes shear-wave solution can be interpreted as a continuous mode). Following a procedure similar to that used by Grosch & Salwen (1978) for the OSE modes, we can show that the discrete and continuous eigenfunctions of the LUBLE (here indicated by the superscript $^{(c)}$) satisfy the biorthogonality relations

$$\left\langle \tilde{\boldsymbol{v}}_{0,n}, \boldsymbol{D}\tilde{\boldsymbol{u}}^{(c)}_{0,k} \right\rangle = \left\langle \tilde{\boldsymbol{v}}^{(c)}_{0,k}, \boldsymbol{D}\tilde{\boldsymbol{u}}_{0,n} \right\rangle = 0, \tag{8.2}$$

$$\left\langle \tilde{\boldsymbol{v}}^{(c)}_{0,k}, \boldsymbol{D}\tilde{\boldsymbol{u}}^{(c)}_{0,k'} \right\rangle = \left\langle \tilde{\boldsymbol{v}}^{(c)}_{0,k'}, \boldsymbol{D}\tilde{\boldsymbol{u}}^{(c)}_{0,k} \right\rangle = \delta(k - k'), \tag{8.3}$$

where $\delta(k - k')$ denotes the Dirac functional. These properties allow us to use the adjoint field like a filter. Suppose we have a numerical solution $\tilde{\boldsymbol{q}}_{num}$ of the parabolic equation (7.7) for some given initial and boundary conditions. Then, sufficiently far downstream of the leading edge (for $\bar{x} \gg 1$), if non-parallel corrections are negligible, we can express $\tilde{\boldsymbol{q}}_{num}$ as the sum of the discrete modes $\tilde{\boldsymbol{u}}_{0,n}$ plus an integral on the path Γ_k over which the continuous spectrum is defined, i.e.

$$\tilde{\boldsymbol{q}}_{num}(X, y) \sim \sum_n C_n(X_i)\tilde{\boldsymbol{u}}_{0,n} \exp(-\mathrm{i}\Theta_n(X, X_i)/\tau) + \int_{\Gamma_k} B_k \tilde{\boldsymbol{u}}^{(c)}_{0,k} \exp(-\mathrm{i}\hat{k}X)\, \mathrm{d}\bar{k} + O(\epsilon_2, \tau), \tag{8.4}$$

where according to (7.14) $\Theta_n(X, X_i) = \int_{X_i}^{X} \bar{\kappa}_n \, \mathrm{d}X$. If we are interested in the coefficient of the kth discrete mode, we can now project $\tilde{\boldsymbol{q}}_{num}$ onto the kth adjoint eigenfunction: in this way, using the biorthogonality relations (8.1), (8.2) and (8.3), we obtain

$$\begin{aligned} \left\langle \tilde{\boldsymbol{q}}^{\dagger}_{0,k}, \boldsymbol{D}\tilde{\boldsymbol{q}}_{num} \right\rangle &\equiv \left\langle \tilde{\boldsymbol{v}}_{0,k} \exp(-\mathrm{i}\Theta_k(X, X_i)/\tau), \boldsymbol{D}\tilde{\boldsymbol{q}}_{num} \right\rangle \\ &\sim \sum_n C_n(X_i)\boldsymbol{\delta}_{k,n} + O(\epsilon_2, \tau) = C_k(X_i) + O(\epsilon_2, \tau). \end{aligned} \tag{8.5}$$

Grosch & Salwen (1978) used a similar technique to extract the coefficients of the Orr–Sommerfeld modes from an unsteady perturbation evolving in a parallel base flow. In the OSE case, the derivation of the biorthogonality conditions is slightly more complicated since the underlying eigenvalue problem is nonlinear. In practice, this difficulty is overcome by reducing the original system to a linear eigenvalue problem through the introduction of extra equations. The augmented system takes on a suitable form to derive the biorthogonality relations from the properties of the adjoint operators.

9. LUBLE eigenfunctions: numerical results

Equation (7.9*a*) is discretized by fourth-order central differences in y on a smoothly varying mesh with the same scheme adopted for the OSE. The second-order horizontal momentum equation is represented at integer collocation points, while the first-order continuity equation is discretized at non-integer collocation points. The vertical momentum equation is reduced by the boundary-layer approximation to the simple equation

$$\frac{\partial p}{\partial y} = 0, \tag{9.1}$$

which can be solved to give $p(X, y) = 0$. The resulting system of algebraic equations is recast in the matrix formulation

$$[\boldsymbol{B}_1 - \mathrm{i}\bar{\alpha}_k \boldsymbol{D}]\tilde{\boldsymbol{u}}_k = \boldsymbol{0}, \tag{9.2}$$

where $\boldsymbol{B}_1$ and $\boldsymbol{D}$ are now block penta-diagonal banded matrices and $\tilde{\boldsymbol{u}}_k$ is a vector containing the unknowns at different grid locations. The homogeneous boundary conditions (7.9c) are inserted in the first two rows of the matrix $\boldsymbol{B}_1$, while at the upper bound of the computational domain the analytical asymptotic solution of (7.9) is enforced to close the system of equations. Right and adjoint eigenvectors and their corresponding eigenvalues are searched with the inverse-iteration algorithm and a study of the sensitivity of the results to the width of the computational domain is performed to detect spurious modes. The eigenfunctions are normalized requiring that $|u(y)|_{max} = 1$ and setting $\langle \tilde{\boldsymbol{v}}, \boldsymbol{D}\tilde{\boldsymbol{u}} \rangle = 1$. It is now convenient to express all the results in terms of quantities non-dimensionalized on the convective wavelength $\ell_c^\star$, i.e. assuming $\tau = 1$. With this choice, the asymptotic solution (7.14) can be rewritten as

$$\tilde{\boldsymbol{q}}_{0,n}(\bar{x}, y) = C_n(\bar{x}_0) \exp\left[-\mathrm{i}\int_{\bar{x}_0}^{\bar{x}} \bar{\kappa}_n \, \mathrm{d}\bar{x}\right] \tilde{\boldsymbol{u}}_{0,n}(\bar{x}, y). \tag{9.3}$$

This expression is the vectorial counterpart of the LR asymptotic eigensolutions whose analytical form is given by Goldstein (1983) in term of the perturbation streamfunction $\bar{\psi}$ as

$$\bar{\psi}_n = C_n^{(G)} \bar{x}^{\tau_n} \left[g_{0,n} + \bar{x}^{-3/2} g_{1,n} + \ldots\right] \exp\left[-\frac{2\lambda_n \bar{x}^{3/2}}{3U_0'}\right] \quad \text{as } \bar{x} \to \infty. \tag{9.4}$$

Here, $C_n^{(G)}$ are undetermined coefficients depending on the initial condition imposed to solve the LUBLE, while the functions $g_{n,0}$ are given by

$$g_{n,0} = \begin{cases} -\mathrm{i}\dfrac{\sqrt{2}U_0'}{\lambda_n} + \sqrt{2\bar{x}} f'(\eta) + O\left(\bar{x}^{-3/2}\right) & \text{for } \eta \sim O(1), \\ \dfrac{\sqrt{2}U_0' \int_0^\sigma (\sigma - \check{\sigma}) w(\check{\sigma}) \, d\check{\sigma}}{\int_0^\infty w(\check{\sigma}) \, d\check{\sigma}} + O(\bar{x}^{-3/2}) & \text{for } \eta \sim O\left(\bar{x}^{-1/2}\right). \end{cases} \tag{9.5}$$

In the previous equations, the following definitions were used

$$U_0' \equiv f''(0) = 0.33205, \tag{9.6a}$$

$$\lambda_n \equiv \mathrm{e}^{-7/4\pi\mathrm{i}} \rho_n^{-3/2}, \tag{9.6b}$$

$$w(\sigma) \equiv \mathrm{Ai}[(\mathrm{i} - \lambda_n \sigma)\mathrm{i}\rho_n], \tag{9.6c}$$

$$\sigma \equiv \sqrt{\bar{x}}\eta = \tilde{y}, \tag{9.6d}$$

$$\tau_n = -\frac{889 - 16\rho_n^3}{1260}, \tag{9.6e}$$

where $-\rho_n$ denotes the nth root of the first derivative of the Airy function Ai. Comparing the multiple-scale solution (9.3) with the analytical form of the eigenfunctions given above and taking into account the different time dependence used,† it is possible to identify the wavenumber $\bar{\kappa}(\bar{x})$ with the simple analytical expression

$$\bar{\kappa}_n^{(G)}(\bar{x}) \equiv \mathrm{i}\frac{\mathrm{d}\ln\left\{x^{\tau_n^*} \exp\left[-\dfrac{\lambda_n^*(2\bar{x})^{3/2}}{3U_0'}\right]\right\}}{\mathrm{d}\bar{x}} = -\mathrm{i}\frac{\lambda_n^*\sqrt{2\bar{x}}}{U_0'} + \mathrm{i}\tau_n^* \frac{1}{\bar{x}}, \tag{9.7}$$

† Goldstein used an $\mathrm{e}^{\mathrm{i}t}$ time dependence while we use $\mathrm{e}^{-\mathrm{i}t}$, so that our results are essentially the complex conjugates of his. Note also that he defined $\eta = y/\sqrt{2X}$ while here $\eta = y/\sqrt{X}$.

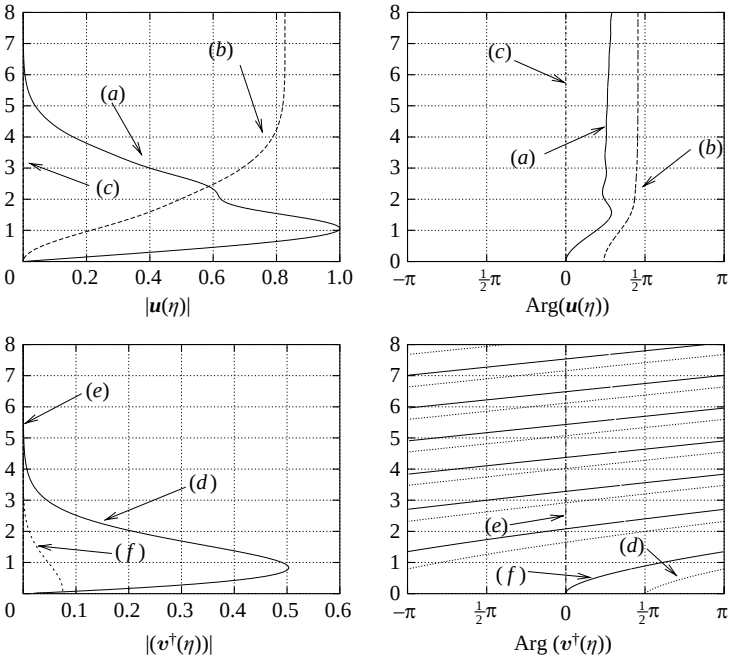

FIGURE 3. Modulus and phase of the first LUBLE eigenfunction and its adjoint at $\bar{x} = 6.0$. The labels refer to the different components of the solution according to: (*a*) u, (*b*) $v/50$, (*c*) p, (*d*) $u^\dagger$, (*e*) $v^\dagger$, (*f*) $p^\dagger$. Note that p and $v^\dagger$ are identically zero.

where the asterisk * denotes complex conjugation. In particular, for the first mode ($n = 1$) we obtain $\lambda_1^* = 0.687632 \times (1 + \mathrm{i})$ and $\tau_1^* = -0.69213$ so that

$$\bar{\kappa}_1^{(G)}(\bar{x}) \equiv 2.07082(1 - \mathrm{i})\sqrt{\bar{x}} - 0.69213\frac{\mathrm{i}}{\bar{x}}. \tag{9.8}$$

Figure 3 displays the various components of the first mode $\tilde{\boldsymbol{u}}(\tilde{y})$ and its adjoint field for a typical value of the streamwise coordinate ($\bar{x} = 6$). The vertical velocity component $\tilde{v}$ is reduced 50 times for convenience. As the numerical solution shows, the shape of the LR modes depends slowly on the streamwise coordinate $\bar{x}$ and consequently the main characteristics of the eigenfunctions remain almost unaltered over the whole spatial domain considered. The upper graphs of figure 4 show the real and imaginary part of the wavenumbers $\bar{\alpha}$, $\bar{\kappa}$ and $\bar{\kappa}^{(G)}$ at different streamwise positions for the first Lam & Rott mode. Non-parallel effects are quite strong in the initial region, but they progressively decrease as we move away from the leading edge. The values of the non-parallel wavenumber $\bar{\kappa}$ predicted by the multiple-scale approach are in excellent agreement with those derived by Goldstein's analytical solution and given in (9.8). The small difference existing in the initial region is probably due to higher-order terms which are taken into account in different ways in the two asymptotic approximations. For $\bar{x}$ larger than 2, however, the two curves are in very close agreement. The lower graphs of figure 4 compare the real and imaginary part of the complex N factor,

$$N(\bar{x}) = \log\left(C(\bar{x})/C_i\right) = -\mathrm{i}\int_{\bar{x}_i}^{\bar{x}} \bar{\kappa}\,\mathrm{d}\bar{x} \tag{9.9}$$

for the first LUBLE eigenfunctions with the corresponding analytical value (indicated here by $N^{(G)}$) obtained by replacing $\bar{\kappa}$ in (9.9) with the analytical value $\bar{\kappa}^{(G)}$ given

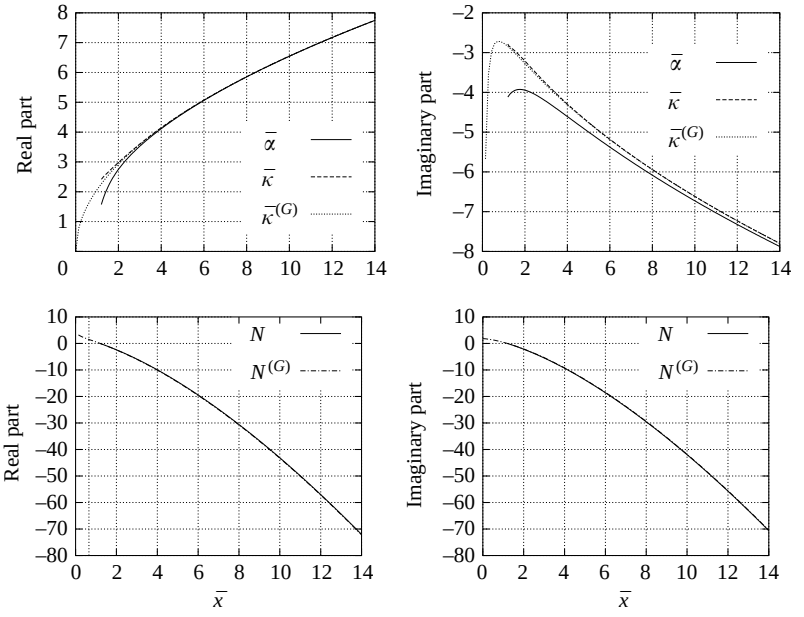

FIGURE 4. Goldstein asymptotics *vs.* multiple-scale expansion ($\bar{x}_0 = 1.2$).

in (9.8). Finally, we conclude this section with a brief discussion on the higher-order modes of the LUBLE. According to the analytic solution found by Lam & Rott, there are an infinite number of eigenfunctions corresponding to the infinite roots of the first derivative of the Airy function Ai. This is not confirmed by the numerical solution of (7.9); in fact, for small values of the streamwise coordinate $\bar{x}$, the eigenvalue solver was able to detect only the first eigenfunction. Higher modes start to appear only at larger values of $\bar{x}$; for example, the second mode is found only for $\bar{x} > 9$, the third for $\bar{x} > 27$ and so on. Figure 5 shows the real and imaginary part of the eigenvalues $\bar{\alpha}_k$ detected in the range $\bar{x} \in [0, 100]$ and the modulus of the horizontal and vertical velocity components for the first three eigenfunctions at $\bar{x} = 50$. The magnitude of the imaginary part of the eigenvalue (which is always negative) becomes smaller and smaller as the order n of the mode is increased, implying smaller streamwise decay rates.

According to these results, the LUBLE behaves in a way similar to the OSE, whose number of modes increases with Re. A possible explanation for the discrepancies in the number of modes predicted by the classical asymptotic theory and our composite asymptotic approach at moderate values of $\bar{x}$ can be found in the form of the analytical solution derived by the matched asymptotic expansion technique. As pointed out by Goldstein *et al.* (1983), at a fixed downstream position, the size of the inner layer tends to increase with the order of the eigenfunction, so that the analytical solutions for the higher modes become accurate only at much larger values of the streamwise coordinate $\bar{x}$. This is actually confirmed by our calculations; note, in fact, how the maximum of the horizontal velocity component tends to move away from the wall as the order of the eigenfunction is increased. In view of these results, the set of Lam & Rott eigenfunctions cannot be complete at finite $\bar{x}$. Brown & Stewartson (1973) found another set of modes of the LUBLE. These eigenfunctions propagate at the free-stream velocity, and the associated disturbances are mainly concentrated near the outer edge of the boundary layer. The Brown–Stewartson modes decay slower than the Lam & Rott eigenfunctions, but their evolution does not seem to lead to the

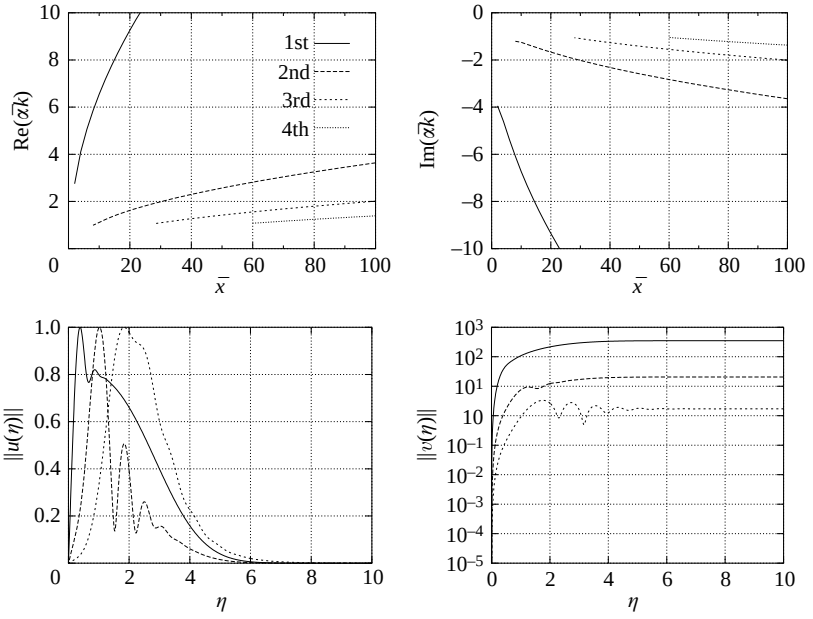

FIGURE 5. Higher modes of the LUBLE.

appearance of unstable disturbances. Their presence in the numerical solution of the linearized unsteady boundary-layer equations has been shown by Hammerton (1999) marching the LUBLE in different sectors of the complex x-plane. The existence of these modes does not invalidate the receptivity analysis of the following sections, but suggests further investigations in order to understand better their role in the evolution of the disturbances and the connection with the discrete and continuous modes of the OSE.

10. Extraction of the receptivity coefficient

The asymptotic methods determine the form of the eigenfunctions but not their coefficients. The receptivity coefficient for any kind of free-stream disturbance can be evaluated only by comparing the numerical solution of (7.4) with its far-field asymptotic behaviour given by (7.14). Problem (7.4) represents a linear parabolic set of differential equations whose solution can be determined with a simple marching strategy. Here, we proceed by discretizing (7.4) in y with the scheme used for the eigenvalue problem (7.9) and solving the resulting semi-discrete equations with a fourth-order fully implicit finite-difference scheme. Another possible approach consists in integrating the equations using the independent variables x and η. In this way, the singularity of the wall normal velocity component at the leading edge can be peeled off and the LUBLE reduce at $\bar{x} = 0$ to a set of ordinary differential equations which can be solved to provide a starting profile for the marching process. Both methods have been used to march the LUBLE in the complex plane and the results were accurately compared. When a sufficient resolution near the leading edge and in the Stokes layer was used, the two numerical approaches returned essentially the same results. The choice between the two methods is therefore just a matter of taste. The semi-similar formulation is probably more accurate when the discretization is performed on a uniform grid. Here, however, a stretched grid with a large number

of grid points has been used to obtain high accuracy and to capture all the details of the solution in the leading-edge region.

To test our extraction procedure based on the adjoint field, we confine our attention to an acoustic free-stream perturbation impinging on the plate at zero angle of attack, which produces a slip velocity and a pressure distribution of the form

$$u_\infty(\bar{x}) = 1, \tag{10.1a}$$

$$\partial p_\infty/\partial \bar{x} = -\mathrm{i}u_\infty(\bar{x}). \tag{10.1b}$$

The initial conditions which must be imposed at the leading edge to start the numerical computations reduce in this case to

$$u_{in}(y) = u_\infty(0), \quad \forall y > 0. \tag{10.2}$$

Once the boundary and the initial conditions are specified, equations (7.4) are marched until the function

$$R_n(\bar{x}, \bar{x}_i) = \left\langle \tilde{\boldsymbol{v}}_{0,n} \exp\left[\mathrm{i}\int_{\bar{x}_i}^{\bar{x}} \bar{\kappa}_n \mathrm{d}\bar{x}\right], \boldsymbol{D}\tilde{\boldsymbol{q}}_{num} \right\rangle \tag{10.3}$$

approaches a constant value: according to (8.5), this number is exactly the coefficient $C_n(X_i)$ in the asymptotic expression (7.14) for the nth eigenfunction. The value of this constant depends on the arbitrary initial point $X_i = \tau\bar{x}_i$ and on the normalization used. To make the results independent of $\bar{x}_i$, it is sometimes better to refer to the total amplitude $T_n^{(LR)}(\bar{x})$, i.e. the amplitude of the eigenfunction at a given final location $\bar{x}$ (see equation (7.14)). In particular, we are interested in determining $C_1(\bar{x}_i)$ (or equivalently $T_1^{(LR)}(\bar{x})$), i.e. the coefficient of the eigensolution which is the precursor of the unstable TS wave. For this purpose, a simple integration along the real axis does not produce the expected results. The function $R_1(\bar{x}, \bar{x}_i)$, in fact, does not tend to a constant value, but shows some oscillations coupled to an exponential growth. A more detailed investigation reveals the nature of the problem. Relation (8.5) is based on the hypothesis that non-parallel effects are negligible or, at least, much smaller than the component we are trying to extract. The biorthogonality relations from which (8.5) is derived are valid only for the leading-order approximation and not for the higher-order correction terms. Thus, if the streamwise variations of the mean flow are larger in magnitude than the leading-order approximation of the first mode, then $R_1(\bar{x}, \bar{x}_i)$ will not represent the receptivity coefficient, but the component of the non-parallel corrections on $\tilde{\boldsymbol{v}}_{0,1}$. This is certainly the case when we march (7.4) on the real axis; non-parallel effects decrease as $\bar{x}$ increases, but simultaneously the contribution of the first eigenfunction to the entire solution decays faster in the streamwise direction owing to the large negative imaginary part of the eigenvalue. A way to solve the problem is to consider the solution of the LUBLE as an analytic function and move the integration path onto a ray in the complex plane where the first eigenfunction is dominant. This procedure, originally suggested by Goldstein *et al.* (1983), has been successfully implemented to extract the receptivity coefficient for several kinds of free-stream disturbances. In order to obtain $C_1(\bar{x}_c)$, the amplitude of the first mode at a given point C on the real axis (see figure 6), we integrate (7.4) along the ray OA until $R_1(\bar{x}, \bar{x}_0)$ becomes constant. Then we use the asymptotic form of the eigenfunction (7.14) to return to the real axis along the path AC and to determine the final amplitude $T_1^{(LR)}(\bar{x}_c)$. Obviously, if the solution really is analytic, different integration paths ending in the same point (such as the paths OAC and OBC) must give the same final result. Several trials have been performed to check the analytic nature of the solution; all theintegrations confirmed this hypothesis and returned roughly the

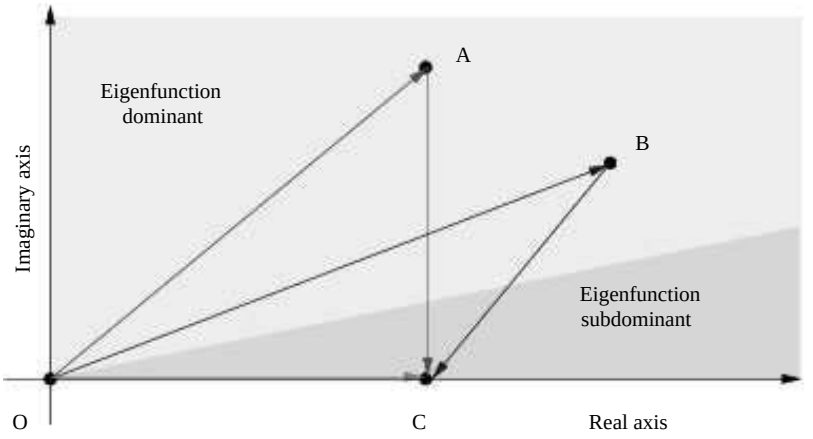

FIGURE 6. Marching in the complex plane.

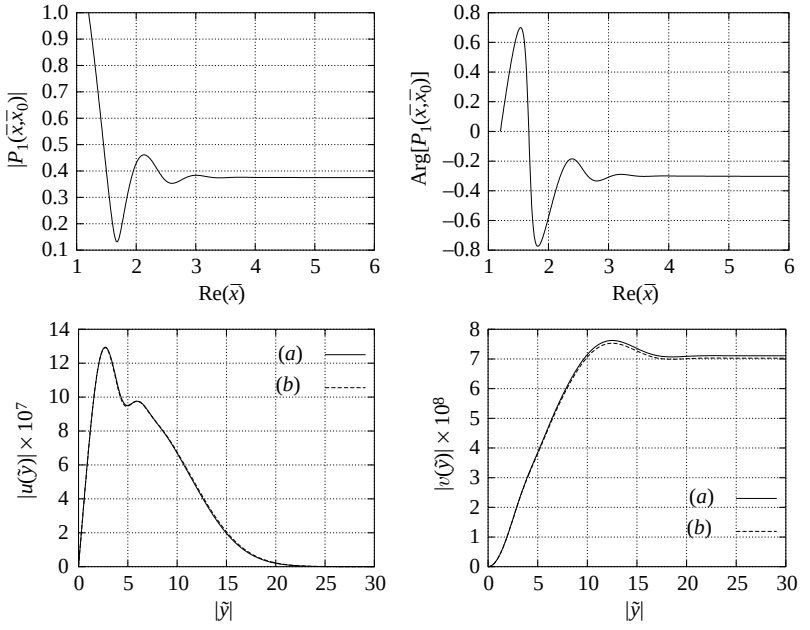

FIGURE 7. The modulus and the phase of the function $P_1(\bar{x}, \bar{x}_0) = R_1(\bar{x}, \bar{x}_0)/R_1(\bar{x}_0, \bar{x}_0)$ and the components of the first eigenfunction in the complex plane: (*a*) marching, (*b*) multiple-scales.

same value for $T_1^{(LR)}(\bar{x}_c)$ (for example we found $T_1^{(LR)}(\bar{x} = 1.2) = -0.01185 + 0.06413\mathrm{i}$ and $T_1^{(LR)}(\bar{x} = 5) = 2.8309 + 1.8639\mathrm{i} \times 10^{-8}$). The upper graphs of figure 7 show the modulus and the phase of $P_1(\bar{x}, \bar{x}_0) = R_1(\bar{x}, \bar{x}_0)/R_1(\bar{x}_0, \bar{x}_0)$ (with $\bar{x}_0 = 1.2 \times (1 + \mathrm{i})$) along a ray with $\mathrm{Arg}(\bar{x}) = \pi/4$: note that this function reaches a constant value at a moderate distance from the origin. The lower graphs instead show the numerical solution of the LUBLE at $\bar{x} = 6+6\mathrm{i}$ and the corresponding asymptotic approximation given by (7.14); it is here evident how the multiple-scale approximation is able to reproduce all the details of the numerical solution. The value of the amplitude at this point in the complex plane is quite large, but it decreases exponentially along the path AC used to return to the real axis. Figures 8 shows the modulus and the

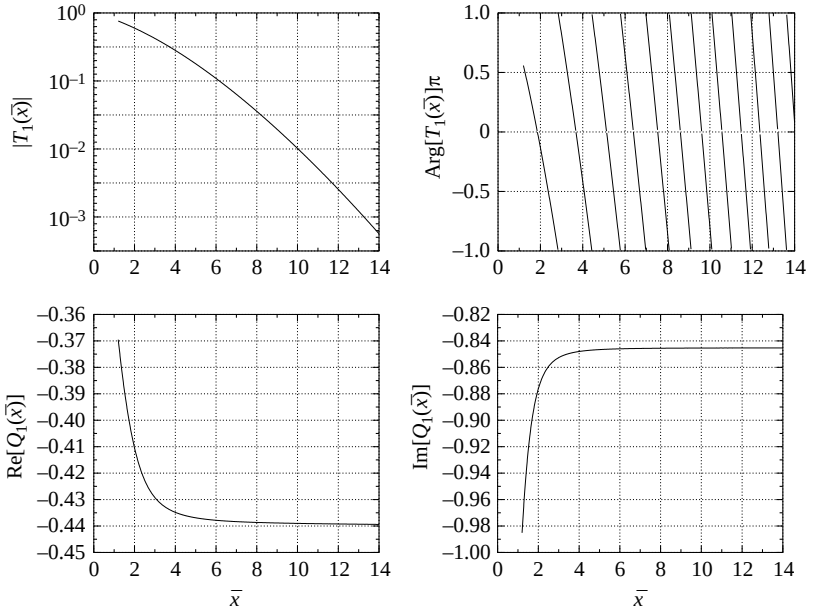

FIGURE 8. The modulus and the phase of the function $T_1(\bar{x})$ on the real x-axis and the real and imaginary parts of the ratio $Q_1(\bar{x})$.

phase of the total amplitude $T_1^{(LR)}(\bar{x})$ at different streamwise stations on the real axis. According to our calculations, the magnitude of the perturbation associated with the first eigenmode is small even in the proximity of the leading edge and decays exponentially as we move further downstream.

In order to make a comparison with the results given by Goldstein *et al.* (1983), we must be able to switch from the normalization adopted here to that implicitly fixed by the analytical solution of the Lam & Rott modes used by Goldstein (1983) and given in (9.5) and (9.6). This can be achieved using the ratio $Q_1(\bar{x})$,

$$Q_1(\bar{x}) = \frac{C_1(\bar{x}_0)\exp\left[-\mathrm{i}\int_{\bar{x}_0}^{\bar{x}}\bar{\kappa}_1 \mathrm{d}\bar{x}\right]\left(\dfrac{\partial \tilde{u}_{0,1}}{\partial \tilde{y}}\right)_{\tilde{y}=0}}{\left(\dfrac{\partial^2 \psi_G}{\partial \tilde{y}^2}\right)_{\tilde{y}=0}} = \frac{T_1^{(LR)}(\bar{x})\left(\dfrac{\partial \tilde{u}_{0,1}}{\partial \tilde{y}}\right)_{\tilde{y}=0}}{\left(\dfrac{\partial^2 \psi_G}{\partial \tilde{y}^2}\right)_{\tilde{y}=0}}, \tag{10.4}$$

between the wall shear predicted by the multiple-scale approach and the corresponding value derived by the analytical solution of the eigenfunctions and given explicitly (see Hammerton & Kerschen 1996, p. 254, equation 3.33) by

$$\left(\frac{\partial^2 \psi_G}{\partial \tilde{y}^2}\right)_{\tilde{y}=0} = \frac{0.4356}{2}(1-\mathrm{i})\exp\left[-\frac{2\lambda_1 \bar{x}^{3/2}}{3U_0'}\right]\bar{x}^{(\tau_1)}. \tag{10.5}$$

In (10.4) $\bar{x}_0$, denotes a chosen starting position while the subscript 1 refers to the mode number. Figure 8 shows the variation of the real and imaginary part of the function $Q_1(\bar{x})$ at different streamwise positions on the real axis. After a short initial stage characterized by a sharp variation, the function $Q_1(\bar{x})$ approaches a constant value, indicating that the results obtained using our numerical procedure and those derived through Goldstein's analytical approach are totally equivalent. In view of this conclusion, the new value assumed by the receptivity coefficient, indicated here as

$C_1^{(G)}$, is found performing the limit

$$C_1^{(G)} = \lim_{x\to\infty} Q_1(\bar{x}). \tag{10.6}$$

According to figure 8, $C_1^{(G)}$ is roughly equal to $-0.439389 - 0.845307\mathrm{i}$, a value in good agreement with the results obtained by Goldstein *et al.* (1983) and by Hammerton & Kerschen (1996, 1997), who, respectively, found $C_1^{(G)} = -0.45 + 0.855\mathrm{i}$ and $C_1^{(G)} = -0.41 + 0.841\mathrm{i}$. (Note that owing to the different time dependence used, our value must be compared with the complex conjugate of theirs.)

11. Matching with the OSE eigenfunction

As pointed out by Goldstein (1983), the wavelength of the Lam & Rott eigenfunctions decreases continuously as they evolve in the streamwise direction. This wavelength-reduction process produces at some downstream location, non-negligible cross-stream pressure fluctuations which invalidate the boundary-layer approximation. In order to roughly locate the region where this occurs, we can take advantage of the numerical results of §9 which show that $\alpha^\star_{LR} \sim \sqrt{\bar{x}}/\ell^\star_c$. With such an assumption and considering that for the Lam & Rott modes $\mathrm{d}/\mathrm{d}x^\star \sim \alpha^\star$ and $\mathrm{d}/dy^\star \sim 1/\delta^\star$, it is easy to show that the asymptotic eigenfunctions are certainly invalid in the region

$$\frac{\omega^\star\delta^\star}{U^\star_\infty}\sqrt{\bar{x}} \sim O(1) \quad \Rightarrow \quad \bar{x} \sim F^{-1/2}. \tag{11.1}$$

Here, and further downstream, the flow is locally parallel, but the pressure terms are not negligible so that the correct asymptotic approximation of the LNSE is given by the stability equations, (5.3) and (5.4). The bound (11.1) can be made more accurate considering the magnitude of the different terms in the LNSE: as pointed out by Goldstein (1983), in fact, the LUBLE breaks down even at smaller value of $\bar{x}$ and precisely for

$$\bar{x} \sim F^{-1/3}, \tag{11.2}$$

which corresponds to the classical triple-deck scaling of the neutral branch. On the other hand, we have seen that the OSE is certainly invalid in the region $\omega x^\star/U^\star_\infty \sim O(1)$; in the leading-edge area, in fact, non-parallel effects are important and the flow is described well by the LUBLE. Figure 9 sketches the different streamwise asymptotic regions of the boundary layer.

We now check the existence and the extension of an overlapping region M, i.e. a region where both approximations are simultaneously valid. Goldstein (1983), using matched asymptotic expansions, showed that in the limit $F \to 0$, the solutions of the OSE match the eigenfunctions of the LUBLE. Since we did not derive analytical solutions of our equations we cannot implement the usual matching strategy. For this reason, we developed a new procedure apt to evaluate finite-Reynolds-number effects and to determine the extent of the overlap domain for different values of the frequency parameter F. To achieve these results, we rely once again on the properties of the adjoint eigenfunctions. Grosch & Salwen (1978) showed that, with a proper normalization, the direct and adjoint nth discrete modes of the Orr–Sommerfeld equations $\boldsymbol{u}_n$ and $\boldsymbol{v}_n$ satisfy the relation

$$\langle \boldsymbol{v}_n \exp(\mathrm{i}\alpha_n x), \boldsymbol{L}\boldsymbol{u}_n \exp(-\mathrm{i}\alpha_n x)\rangle = 1 \quad \forall \mathrm{x}, \tag{11.3}$$

where $\boldsymbol{L} = \mathrm{i}(\partial \boldsymbol{H}_{OS}/\partial\alpha)$ is the operator given in (A 2). For a parallel mean-flow profile, $\boldsymbol{u}\mathrm{e}^{-\mathrm{i}\alpha x}$ and $\boldsymbol{v}\mathrm{e}^{\mathrm{i}\alpha x}$ represent, respectively, the exact solutions of the linearized

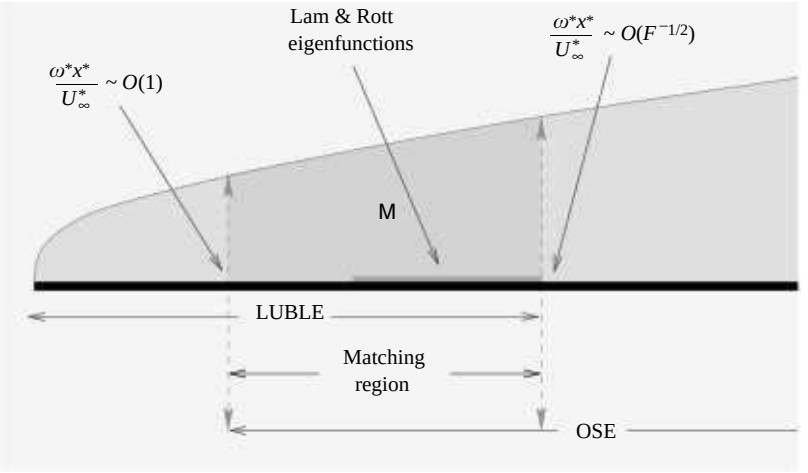

FIGURE 9. The different asymptotic approximations and the matching region.

Navier–Stokes operator and of its adjoint. Relation (11.3) can be extended to include cases in which the base flow is slowly varying in the streamwise direction. In these circumstances, the leading-order solutions for the direct and adjoint nth modes of the LNSE are given by (5.8) and (5.10). Thus, from (11.3), the amplitude $A_n(X_0)$ of the nth TS eigenfunction can be retrieved at different streamwise positions by projecting $\boldsymbol{q}_n^{(LNSE)}$ onto $\boldsymbol{q}_n^{\dagger(LNSE)}$, i.e.

$$\left\langle \boldsymbol{q}_n^{\dagger(LNSE)}, \boldsymbol{L}\, \boldsymbol{q}_n^{(LNSE)} \right\rangle = A_n(X_0). \tag{11.4}$$

We now use this property to check the existence and the extent of the overlapping region M. By definition, in this area the asymptotic solution of the LUBLE must asymptotically match the solution of the OSE (5.8), i.e.

$$\boldsymbol{q}_n^{(LNSE)}(X, y) - \boldsymbol{q}_n^{(LUBLE)}(X, y) \to 0 \qquad \text{as } F \to 0 \quad \forall y, \tag{11.5}$$

where $\boldsymbol{q}_n^{(LUBLE)}(X, y)$ is explicitly given by (7.16). Considering (7.16), we can therefore define the overlap domain M as the set

$$\mathsf{M} = \left\{ X : \left\langle \boldsymbol{q}_n^{\dagger(LNSE)}, \boldsymbol{L}\, \boldsymbol{q}_n^{(LUBLE)} \right\rangle \approx \text{cost} \right\}. \tag{11.6}$$

Using the analytic form of the two solutions, it is useful to rewrite the projection as

$$\left\langle \boldsymbol{q}_n^{\dagger(LNSE)}, \boldsymbol{L}\, \boldsymbol{q}_n^{(LUBLE)} \right\rangle = C_n(\bar{x}_0) M_n(\bar{x}, \bar{x}_0), \tag{11.7}$$

where $C_n(\bar{x}_0)$ is the coefficient of the nth Lam & Rott eigenfunction, $M_n(\bar{x}, \bar{x}_0)$ is the function

$$M_n(\bar{x}, \bar{x}_0) = \left\langle \boldsymbol{v}_{0,n}^{\dagger(OS)}, \boldsymbol{L}\, \boldsymbol{u}_{0,n}^{(LR)} \right\rangle \exp\left[\int_{\bar{x}_0}^{\bar{x}} \bar{\kappa}_n^{(OS)} - \bar{\kappa}_n^{(LR)} \mathrm{d}\bar{x} \right]. \tag{11.8}$$

and the superscripts $^{(OS)}$ and $^{(LR)}$ refer, respectively, to the Orr–Sommerfeld and Lam & Rott modes. The function (11.8) measures the accuracy of the approximation obtained by replacing the nth TS mode with the nth Lam & Rott eigenfunction. The presence of the exponential term in (11.8) produces a sensible streamwise growth (or decay) of $M_n(\bar{x}, \bar{x}_0)$ wherever a considerable difference between the two wavenumbers is found. From a practical point of view, the existence and the extent of a matching region can therefore be studied by monitoring the behaviour of $M_n(\bar{x}, \bar{x}_0)$ and identifying an area over which this function assumes approximately a constant

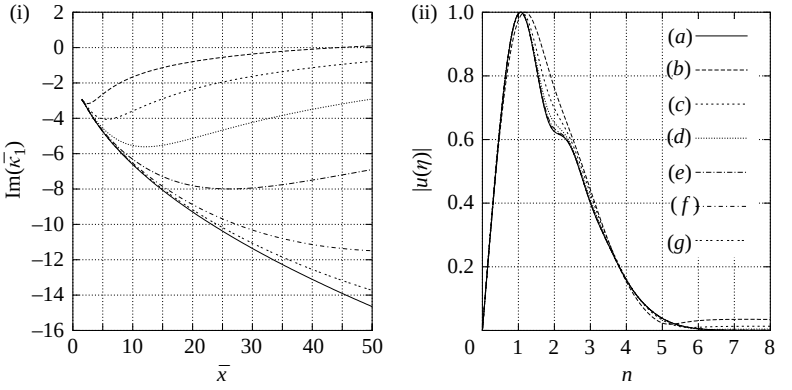

FIGURE 10. Imaginary part of $\bar{\kappa}_1^{(LNSE)}$ and $\bar{\kappa}_1^{(LUBLE)}$ and modulus of the corresponding horizontal velocity components at $\bar{x} = 6$ for several values of the frequency parameter F: (*a*) *LUBLE*, (*b*) $F = 1.0 \times 10^{-6}$, (*c*) $F = 1.0 \times 10^{-7}$, (*d*) $F = 1.0 \times 10^{-8}$, (*e*) $F = 1.0 \times 10^{-9}$, (*f*) $F = 1.0 \times 10^{-10}$, (*g*) $F = 1.0 \times 10^{-11}$.

value. In particular, for $n = 1$, the amplitude of the unstable TS wave $A_1(\bar{x}_0)$ can be retrieved in M by multiplying $M_1(\bar{x}, \bar{x}_0)$ with the value of the receptivity coefficient $C_1(\bar{x}_0)$ previously extracted. In this way, it is possible to decouple the matching procedure from the receptivity calculations. Once the extension of the matching region has been studied, the total amplitude $T^{(OS)}(\bar{x})$ of the unstable TS wave at some downstream position can be evaluated using

$$T^{(OS)}(\bar{x}) \equiv A(x_0) \exp\left[\int_{\bar{x}_0}^{\bar{x}} \bar{\kappa}_n^{(OS)} \mathrm{d}\bar{x}\right] = C_1(\bar{x}_0) M_1(\bar{x}_1, \bar{x}_0) \exp\left[\int_{\bar{x}_1}^{\bar{x}} \bar{\kappa}_n^{(OS)} \mathrm{d}\bar{x}\right], \qquad (11.9)$$

where $\bar{x}_1 \in \mathsf{M}$. According to our non-dimensionalization, $T^{(OS)}(\bar{x})$ represent, the maximum value of the streamwise velocity component of the TS wave non-dimensionalized on the free-stream perturbation amplitude.

In figure 10(i) we compare the imaginary part of the wavenumbers $\kappa_1^{(OS)}$ and $\kappa_1^{(LR)}$, non-dimensionalized on the convective wavelength $\ell_c^\star$, for several values of the frequency parameter F, while in figure 10(i) we show the modulus of the horizontal velocity components of the OSE and LUBLE eigenfunctions at $\bar{x} = 6$. From a graphical point of view it is clear that the two asymptotic solutions tend to match as $F \to 0$. A more quantitative analysis is provided by figures 11 and 12, which show the modulus of the function $M_1(\bar{x}, \bar{x}_0)$ (with $\bar{x}_0 = 1.05$) for values of the frequency parameter in two different ranges. In figure 10(ii), a smaller streamwise domain has been used in order to show better the behaviour of the function in the region close to the leading edge. According to our results, a definite matching region exists only for values of the frequency parameter smaller than 10^{-6}. In such cases, the width of the overlap domain tends to increase progressively as F is lowered. On the other hand, for values of F larger than 10^{-6}, no matching is clearly visible. This behaviour indicates that terms neglected in the derivation of the LUBLE are still important in the leading-edge area. Although not very accurate in this circumstance, the asymptotic procedure based on the complementary approximation (7.3) can still be used to perform quantitative analysis of the receptivity process. Note, in fact, that for all values of F, the curves representing $|M_1(\bar{x}_0, \bar{x})|$ tend to flatten as the leading edge is approached, showing that the Lam & Rott eigensolutions best approximate the OSE modes in this part of the boundary layer. This behaviour suggests performing

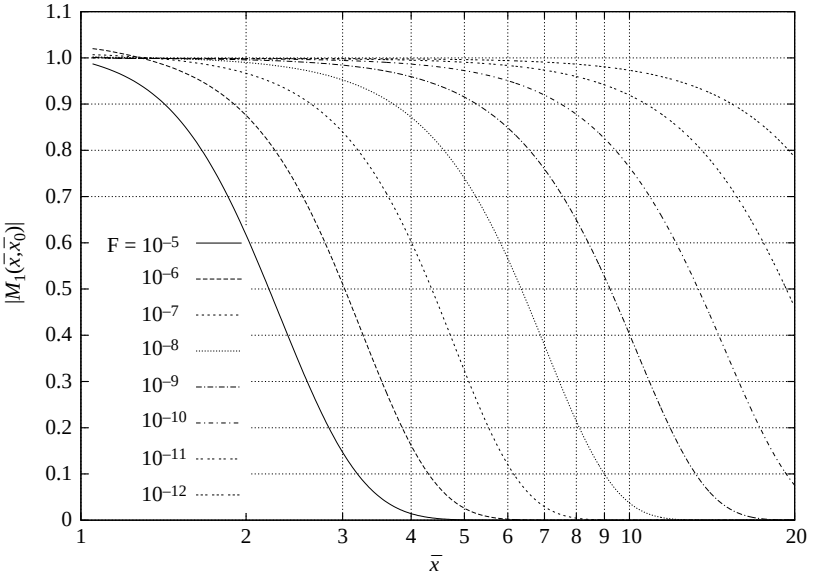

FIGURE 11. Modulus of $M_1(\bar{x}, \bar{x}_0)$ for different values of F ($\bar{x}_0 = 1.05$).

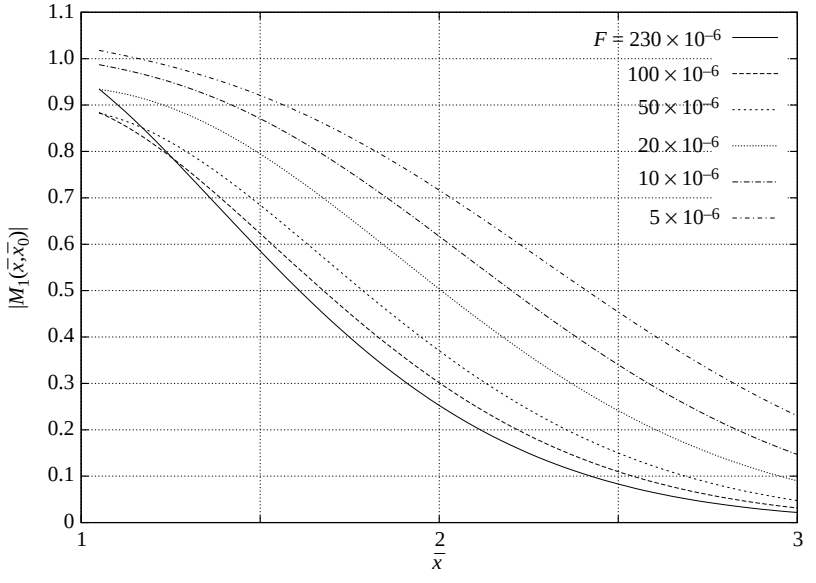

FIGURE 12. Modulus of $M_1(\bar{x}, \bar{x}_0)$ for different values of F ($\bar{x}_0 = 1.05$).

the matching as close as possible to the leading edge; in this way the error due to terms neglected in the boundary-layer approximation can be minimized. As an example of this procedure, figure 13 shows the total amplitude of the TS wave generated by the leading-edge receptivity process at different streamwise positions and for different values of the frequency parameter F. The data refer to the case of an acoustic wave impinging horizontally on the flat plate. The matching has been performed at $\bar{x}_1 = \bar{x}_0 = 1.05$, i.e. using the closest point to the leading edge for which we could determine the Lam & Rott eigenfunctions. If the value of $\bar{x}_1$ is

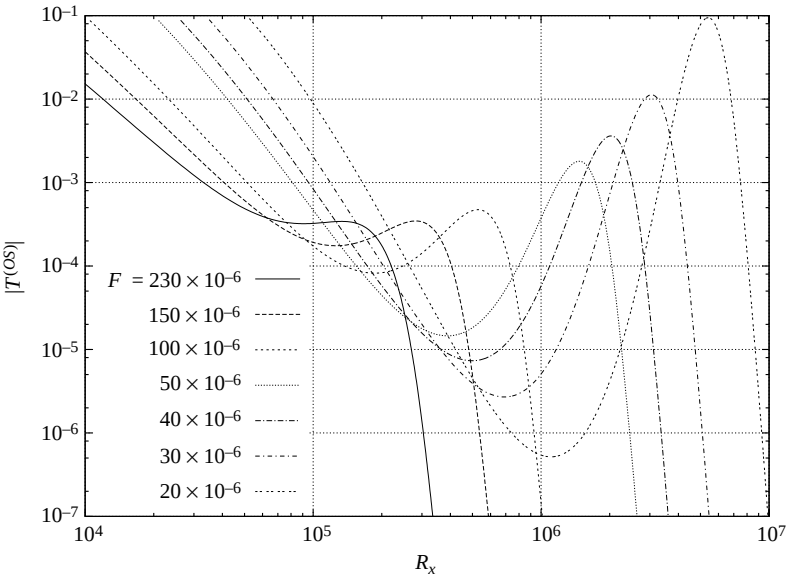

FIGURE 13. Amplitude of TS waves non-dimensionalized on the free-stream value of the perturbation at different Reynolds numbers R_x.

further decreased, in fact, the eigenvalue solver exhibits a slow convergence and, at the end, fails to detect the eigenfunction jumping towards a spurious solution. The range of frequencies investigated is quite common in practical applications, but at the same time corresponds to the case for which the numerical matching procedure based on the adjoint eigenfunctions is less reliable (as shown in figure 12, in fact, no overlap domain exists for these frequencies). As F is lowered, the neutral points move downstream while the amplification region tends to enlarge. As a result, the amplitude at branch II depends on the decay and growth rate experienced by the wave in these different regions of the boundary layer. The higher values of F considered in figure 13 correspond to cases close to the top of the neutral stability loop. The amplitudes at the first neutral point are not extremely small since, for these waves, the region upstream of the neutral branch is quite short. On the other hand, the width of the amplification region is limited and consequently the amplitude at the second branch is still small. The TS waves corresponding to the lower frequencies experience, instead, a stronger decay rate before reaching the first branch, but this is compensated by a larger amplification region. The higher frequency in figure 13 is $F = 230 \times 10^{-6}$ and corresponds to the worst case among those considered in this paper for the numerical matching procedure. The same frequency has been used by Haddad & Corke (1998) to study the effect of the nose radius on the leading-edge receptivity process. We can therefore test our numerical matching procedure comparing our results with those obtained through DNS. Unfortunately, Haddad & Corke (1998) do not give the maximum amplitude of the perturbation associated with the TS wave at branches I and II for the zero-Strouhal-number case. This information can be retrieved by considering figure 13 (*b*) of their paper and comparing the magnitude of the local oscillations at a given height above the wall with the shape of the local eigenfunction. In this way, we obtained at branch II $|T^{(OS)}(\bar{x}_{N_{II}})| \approx 3.57 \times 10^{-4}$, a value in good agreement with the result based on our asymptotic approach, which instead returned $|T^{(OS)}(\bar{x}_{N_{II}})| \approx 3.43 \times 10^{-4}$.

Case	Present study	Wanderley & Corke (2001)	Saric & White (1998)
Geometry	Flat plate	MSE 20:1	MSE 20:1
$F \times 10^6$	90	90	88-92
$\lvert T^{(OS)}(x_{N_I})\rvert$	6.5×10^{-5}	0.046	0.050 ± 0.005

TABLE 4. Branch I TS amplitude for the 20:1 MSE and a flat plate.

According to figure 13, for frequencies of interest in practical applications, the amplitude is in the range [0.001 : 0.1]. Assuming now that for a disturbance that might contribute to transition, its branch II amplitude is about 1% of $U_\infty^\star$, these results suggest that for this particular case it is unlikely to observe transition owing to perturbations generated by a linear mechanism at the leading-edge. This, however, does not mean that the leading-edge mechanism is irrelevant to the transition process. In fact, other kinds of disturbance can produce much larger receptivity coefficients; Kerschen *et al.* (1990), for example, showed that oblique sound waves can give rise to unstable waves an order of magnitude larger than those produced by acoustic disturbances propagating parallel to the plate. Moreover, for more complex geometries, the existence of an adverse pressure gradient region close to the leading edge might considerably affect the growth or decay rate of the perturbation inside the boundary layer. An example of this effect is offered by the receptivity on a finite-thickness flat plate with an elliptical leading edge. The ellipse has an adverse pressure gradient region and two sites of receptivity, one at the leading edge and one at the point where the ellipse joins the flat plate. In order to minimize the effect of the joint, Saric, Wei & Rasmussen (1995) and Saric & White (1998) used a 'modified super ellipse' (MSE). This has a variable exponent for the ellipse long axis to give zero curvature at the joint location. Wanderley & Corke (2001) studied this configuration performing a direct numerical simulation of the LNSE. Good agreement was found with the experimental results obtained by Saric *et al.* (1995) and Saric & White (1998). Table 4 compares the TS amplitude at branch I for the modified super ellipse with aspect ratio 20:1 and a simple flat plate. The data show that branch I amplitudes for the finite-thickness flat plate are about three orders of magnitude larger than those for the infinitely thin flat plate, confirming the strong influence of the adverse pressure gradient region located at the joint between the plate and the mse.

12. Conclusions

In this paper we have developed a new numerical technique for the extraction of the receptivity coefficient which is easy to apply even in complex flow configurations. The two streamwise asymptotic regions into which the boundary layer is divided are studied with a unified approach based on the determination of composite differential equations describing the local properties of the flow field. This is achieved by applying a multiple-scale expansion to the governing equations and rearranging higher-order terms in a way that to builds regular leading-order problems. Non-parallel corrections due to the slow streamwise growth of the base flow are taken into account by imposing a solvability condition on the higher-order problems. The resulting eigenvalue problems are solved numerically with a simple iterative algorithm. The biorthogonality properties of the adjoint operators are then used to extract the receptivity coefficient and to match the LUBLE and the OSE eigenfunctions. The extent of the matching region is evaluated numerically for different values

of the frequency parameter in order to highlight the equivalence of the asymptotic approximations used in the different regions of the boundary layer. This new procedure has been tested for the case of an acoustic wave impinging on an incompressible flat-plate boundary layer, and results have been compared with those derived by Goldstein (1983), Goldstein *et al.* (1983) and Hammerton & Kerschen (1996, 1997). Numerical results show that in the lower frequency range, a definite matching region is clearly visible, but this shortens progressively as F is increased. At moderate values of F, instead, no matching exists; in these circumstances, in fact, the pressure fluctuations, neglected in the derivation of the LUBLE, are still important in the leading-edge area and must be properly taken into account whenever a precise estimate of the receptivity coefficient is sought. In these cases, although not very accurate, the novel matching procedure can still be used to obtain quantitative information about the amplitude of the generated TS waves. This is achieved by performing the matching as close as possible to the leading edge, in order to minimize the error due to the boundary-layer approximation. Using this procedure, we evaluated at different streamwise locations and for different values of F, the amplitude of the perturbation associated with the TS wave generated by an acoustic wave impinging horizontally on the flat plate. A comparison of the results at $F = 230 \times 10^{-6}$ with the DNS data of Haddad & Corke (1998) has shown good quantitative agreement. These preliminary results seem to indicate that the numerical asymptotic approach presented in this paper can be used to obtain qualitative and quantitative information on the receptivity process in a range of frequencies of interest for practical applications, without necessarily relying on the more expensive DNS approach.

The authors wish to acknowledge a number of helpful discussions at DAMTP with Professor Nigel Peake. We also would like to thank Professor Haddad to provide us the DNS data used for the comparison. F. G. has been supported by the EU under the Marie Curie Fellowship Programme.

Appendix A. Details of the stability operators

The operators $\boldsymbol{H}_{OS}(\omega, \alpha, Re)$, $\boldsymbol{L}(\alpha, Re)$ and $\boldsymbol{M}(\alpha, Re, \epsilon_1)$ involved in problems (5.3) and (5.4) are derived from the multiple-scale expansion (5.2). In particular $\boldsymbol{H}_{OS}(\omega, \alpha, Re)$ is the classical Orr–Sommerfeld operator

$$\boldsymbol{H}_{OS} = \begin{bmatrix} \mathrm{i}(\omega - \alpha U_B) + \dfrac{1}{Re}\left(\alpha^2 - \dfrac{\partial^2}{\partial y^2}\right) & \dfrac{\partial U_B}{\partial y} & -\mathrm{i}\alpha \\ 0 & \mathrm{i}(\omega - \alpha U_B) + \dfrac{1}{Re}\left(\alpha^2 - \dfrac{\partial^2}{\partial y^2}\right) & \dfrac{\partial}{\partial y} \\ -\mathrm{i}\alpha & \dfrac{\partial}{\partial y} & 0 \end{bmatrix}, \tag{A 1}$$

while $\boldsymbol{L}(\alpha, Re)$ and $\boldsymbol{M}(\alpha, Re, \epsilon_1)$ are defined, respectively, by

$$\boldsymbol{L} = \mathrm{i}\frac{\partial \boldsymbol{H}_{OS}(\alpha)}{\partial \alpha} = \begin{bmatrix} U_B + \dfrac{2\mathrm{i}\alpha}{Re} & 0 & 1 \\ 0 & U_B + \dfrac{2\mathrm{i}\alpha}{Re} & 0 \\ 1 & 0 & 0 \end{bmatrix} \tag{A 2}$$

and

$$\boldsymbol{M}(\alpha, Re, \epsilon_1) = \boldsymbol{M}_1(\alpha, Re) + \frac{\varepsilon}{\epsilon_1}\boldsymbol{M}_2, \tag{A 3}$$

with

$$\boldsymbol{M}_1 = \begin{bmatrix} \mathrm{i}\,\dfrac{\partial\alpha}{Re\,\partial X_1} & 0 & 0 \\ 0 & \mathrm{i}\,\dfrac{\partial\alpha}{Re\,\partial X_1} & 0 \\ 0 & 0 & 0 \end{bmatrix} \tag{A 4}$$

and

$$\boldsymbol{M}_2 = \begin{bmatrix} \dfrac{\partial U_B}{\partial X} + V_B\dfrac{\partial}{\partial y} & 0 & 0 \\ 0 & \dfrac{\partial V_B}{\partial y} + V_B\dfrac{\partial}{\partial y} & 0 \\ 0 & 0 & 0 \end{bmatrix}. \tag{A 5}$$

Inspection of (A 1) reveals that the leading-order problem (5.3*a*) contains terms (those multiplied by $\varepsilon = Re^{-1}$) which vanish in the limit $\varepsilon \to 0$. Removing these terms, however, leads to a singular problem, since the highest derivatives in y of the Orr–Sommerfeld operator are lost and with them disappears the possibility of enforcing a certain number of boundary conditions. In a classical approach, this problem is overcome by the use of a multi-deck expansion which provides a link between the two parameters ϵ_1 and ε. In this paper, however, the aim is to build a uniformly valid approximate differential equation by combining together all terms that are dominant in at least one of these decks, or, in other words, by retaining those components which would lead to a singular problem if omitted. Since moving terms from higher to lower orders does not alter the general accuracy of the approximation, the composite asymptotic expansion (5.2) and the resulting composite equation are not uniquely determined. Here, we decided to retain at $O(\epsilon_1^0)$ only those terms in ε and ϵ_1 that do not vanish for a truly parallel mean flow. Other choices are, however, possible; we tested some of them to check the differences. Substantial deviations in the results were observed only in a region close to the leading edge where the multiple-scale approximation is not valid anyway.

Appendix B. Details of LUBLE operators

The operators $\boldsymbol{D}$, $\boldsymbol{B}_1(Sr)$ and $\boldsymbol{B}_2(Sr, \tau, \epsilon_2)$ involved in (7.7) are defined as

$$\boldsymbol{D} = \begin{bmatrix} U_B & 0 & 0 \\ 0 & 0 & 0 \\ 1 & 0 & 0 \end{bmatrix}, \tag{B 1}$$

$$\boldsymbol{B}_1 = \begin{bmatrix} \mathrm{i} - \dfrac{1}{Sr}\dfrac{\partial^2}{\partial y^2} & \dfrac{1}{Sr}\dfrac{\partial U_B}{\partial y} & 0 \\ 0 & 0 & \dfrac{\partial}{\partial y} \\ 0 & \dfrac{1}{Sr}\dfrac{\partial}{\partial y} & 0 \end{bmatrix} \tag{B 2}$$

and

$$\boldsymbol{B}_2 = \frac{\tau}{\epsilon_2}\begin{bmatrix} \dfrac{\partial U_B}{\partial X} + \mathrm{V}_B\dfrac{\partial}{\partial y} & 0 & 0 \\ 0 & 0 & 0 \\ 0 & 0 & 0 \end{bmatrix}. \tag{B 3}$$

Note that $\boldsymbol{B}_1$ contains terms which involve neither the streamwise derivatives of the fluctuation quantities, grouped in the operator $\boldsymbol{D}$, nor terms including V_B or the streamwise derivatives of the mean flow, which are instead listed in $\boldsymbol{B}_2$. With this choice, the two problems (7.9) and (7.10), describing the far-field behaviour of the LUBLE and obtained using the multiple-scale expansion (7.8), can be directly derived from (5.3) and (5.4) neglecting in the operators $\boldsymbol{H}_{OS}$, $\boldsymbol{L}$, $\boldsymbol{M}_1$ and $\boldsymbol{M}_2$ those terms which are of higher order in a boundary-layer approximation. With the previous definitions, the leading-order problem (7.9) contains terms which are formally $O(\tau)$. From a practical point of view, the minimal composite regular problem is obtained by retaining at leading order only the second derivative of u and the term involving $\tilde{v}$ in the momentum equation, and the first derivative of $\tilde{v}$ in the continuity equation. Keeping other $O(\tau)$ terms does not modify the overall order of accuracy of the approximation, but leads to a different leading-order problem. As for the OSE, numerical results have confirmed the equivalence of all these formulations: important differences, in fact, were observed only in a small region around $Sr \sim 1$, where the multiple-scale approximation breaks down. The leading-order problem chosen for the present analysis is particularly convenient: in fact, from a numerical point of view, problems (7.9) and (7.10) can be derived and solved with simple algebraic manipulations of the matrices used to march the parabolic equation (7.7).

REFERENCES

Ackerberg, R. C. & Phillips, J. H. 1972 The unsteady laminar boundary layer on a semi-infinite flat plate due to small fluctuations in the magnitude of free-stream velocity. *J. Fluid Mech.* **51**, 137–157.

Bender, C. M. & Orszag, S. A. 1978 *Advanced Mathematical Methods for Scientists and Engineers.* McGraw–Hill.

Bodonyi, R. J. & Smith, F. T. 1981 The upper branch stability of the Blasius boundary layer, including non-parallel flow effects. *Proc. R. Soc. Lond.* **375**, 65–92.

Bottaro, A. & Luchini, P. 1999 Görtler vortices: are they amenable to local eigenvalue analysis? *Eur. J. Mech.* B/*Fluids* **18**, 47–65.

Brown, S. N. & Stewartson, K. 1973 On the propagation of disturbances in a laminar boundary layer. *Proc. Camb. Phil. Soc.* **73**, 493–514.

Casalis, G., Gouttenoire, C. & Troff, B. 1997 DNS Investigation of leading edge and localized receptivity. In *Proc. First AFOSR Intl Conf. on DNS/LES. Louisiana Tech. University, Ruston, Louisiana, USA*. Greyden Press, Colombus.

Erturk, E. & Corke, T. C. 2001 Boundary-layer leading-edge receptivity to sound at incidence angles. *J. Fluid Mech.* **444**, 383–407.

Fedorov, A. V. 2003 Receptivity of a high-speed boundary layer to acoustic disturbances. *J. Fluid Mech.* **491**, 101–129.

Fedorov, A. V. & Khokhlov, A. P. 1991 Excitation of unstable modes in a supersonic boundary layer by acoustic waves. *Fluid Dyn.* **4**, 67–74.

Fedorov, A. V. & Khokhlov, A. P. 1993 Excitation and evolution of unstable disturbances in supersonic boundary layer. *Proc. ASME, Fluid Engng Conf. Washington, DC*, vol. 151, pp. 1–13.

Gaster, M. 1974 On the effects of boundary layer growth on flow stability. *J. Fluid Mech.* **66**, 465–480.

Goldstein, M. E. 1983 The evolution of Tollmien–Schlichting waves near a leading edge. *J. Fluid Mech.* **127**, 59–81.

Goldstein, M. E., Sockol, P. M. & Sanz, J. 1983 The evolution of Tollmien–Schlichting waves near a leading edge. Part 2. Numerical determination of the amplitude. *J. Fluid Mech.* **129**, 443–453.

Goldstein, S. 1956 Flow of an incompressible viscous fluid along a semi-infinte flat plate. *Tech. Rep.* HE-150-144. Engng Res. Inst. Univ. Calif.

Goldstein, S. 1960 *Lectures on Fluid Mechanics*. Wiley (Interscience).

Govindarajan, R. & Narasimha, R. 1997 A low order theory for stability of non-parallel boundary layer flows. *Proc. R. Soc. Lond.* **453**, 2537–2549.

Govindarajan, R. & Narasimha, R. 1999 A low-order parabolic theory for boundary-layer stability. *Phys. Fluids* **11**, 1449–1458.

Govindarajan, R. & Narasimha, R. 2001 Estimating amplitude ratios in boundary layer stability theory: a comparison between two approaches. *J. Fluid Mech.* **439**, 403–412.

Grosch, C. E. & Salwen, H. 1978 The continuous spectrum of the Orr–Sommerfeld equation. Part 1. The spectrum and the eigenfunctions. *J. Fluid Mech.* **87**, 33–54.

Grosch, C. E. & Salwen, H. 1981 The continuous spectrum of the Orr–Sommerfeld equation. Part 2. Eigenfunction expansion. *J. Fluid Mech.* **104**, 445–465.

Haddad, O. M. & Corke, T. C. 1998 Boundary layer receptivity to free stream sound on parabolic bodies. *J. Fluid Mech.* **368**, 1–26.

Hammerton, P. W. 1999 Comparison of Lam–Rott and Brown–Stewartson eigensolutions of the boundary-layer equations. *Q. J. Mech. Maths* **52**, 373–385.

Hammerton, P. W. & Kerschen, E. J. 1996 Boundary-layer receptivity for a parabolic leading edge. *J. Fluid Mech.* **310**, 243–267.

Hammerton, P. W. & Kerschen, E. J. 1997 Boundary-layer receptivity for a parabolic leading edge. Part 2. The small-Strouhal-number limit. *J. Fluid Mech.* **353**, 205–220.

Heinrich, R. A. 1989 Flat-plate leading-edge receptivity to various free-stream disturbance structures. PhD thesis, University of Arizona.

Heinrich, R. A. & Kerschen, E. J. 1989 Leading-edge boundary-layer receptivity to various free-stream disturbance structures. *Z. Angew. Math. Mech.* **69**, 596–598.

Hinch, E. J. 1994 *Perturbation Methods.*. Cambridge University Press.

Kerschen, E. J., Choudhari, M. & Heinrich, R. A. 1990 Generation of boundary instability waves by acoustic and vortical freestream disturbances. In *Laminar–Turbulent Transition*, vol. 3 (ed. D. Arnal & R. Michel). Springer.

Lam, S. H. & Rott, N. 1960 Theory of linearized time-dependent boundary layers. *Rep. AFOSR* TN-60-1100. Cornell University, Grad. School of Aero. Engng.

Lam, S. H. & Rott, N. 1993 Eigenfunctions of linearized unsteady boundary layer equations. *Trans. ASME* I: J. Fluids Engng **115**, 597–602.

Ma, Y. & Zhong, X. 2003*a* Receptivity of a supersonic boundary layer over a flat plate. Part 1. Wave structures and interactions. *J. Fluid Mech.* **488**, 31–78.

Ma, Y. & Zhong, X. 2003*b* Receptivity of a supersonic boundary layer over a flat plate. Part 2. Receptivity to free-steram sound. *J. Fluid Mech.* **488**, 79–121.

Morse, P. M. & Feshbach, H. 1953 *Methods of Theoretical Physics,* Part 1. McGraw–Hill.

Narasimha, R. & Govindarajan, R. 2000 Minimal composite equations and the stability of non-parallel flows. *Current Sci.* **79**, 730–740.

Ruban, A. I. 1984 On the generation of Tollmien–Schlichting waves by sound. *Fluid Dyn.* **19**, 709–717.

Saric, W. S. & Nayfeh, A. H. 1975 Non-parallel stability of boundary-layer flows. *Phys. Fluids* **18**, 945–950.

Saric, W. S., Reed, H. L. & Kerschen, E. J. 2002 Boundary-layer receptivity to freestream disturbances. *Annu. Rev. Fluid Mech.* **39**, 291–319.

Saric, W. S., Wei, W. & Rasmussen, B. K. 1995 Effect of leading-edge on sound receptivity. *Laminar–Turbulent Transition*, vol. 4.

Saric, W. S. & White, E. B. 1998 Influence of high-amplitude noise on boundary-layer transition to turbulence. *AIAA Paper* 98-2645.

Smith, F. T. 1979*a* On the non-parallel flow stability of the Blasius boundary layer. *Proc. R. Soc. Lond.* **366**, 91–109.

Smith, F. T. 1979b Nonlinear stability of boundary layers for disturbances of various size. *Proc. R. Soc. Lond.* **368**, 573–589.

Stewartson, K. 1969 On the flow near the trailing edge of a flat plate. Part II. *Mathematika* **16**, 106–121.

Stewartson, K. 1974 Multistructured boundary layers on flat plates and related bodies. *Adv. Appl. Mech.* **370**, 149–174.

Van Dyke, M. D. 1964 *Perturbation Methods in Fluid Mechanics.* Academic.

Wanderley, J. B. V. & Corke, T. C. 2001 Boundary-layer receptivity to freestream sound on elliptic leading edges of flat plates. *J. Fluid Mech.* **429**, 1–29.

Zhong, X. 2001 Leading-edge receptivity to free-stream disturbance waves for hypersonic flow over a parabola. *J. Fluid Mech.* **441**, 315–367.